이학박사 학위논문

나노갭의 능동적 및 수동적 조작을 통한 광학적 및 전기화학적 응용에 관한 연구

Active and passive control of nanogaps for optical and electrochemical applications

2019년 8월

서울대학교 대학원
물리천문학부
윤 형 석

나노갭의 능동적 및 수동적 조작을 통한 광학적 및 전기화학적 응용에 관한 연구

Active and passive control of nanogaps for optical and electrochemical applications

지도교수 홍 성 철

이 논문을 이학박사 학위논문으로 제출함

2019년 8월

서울대학교 대학원

물리천문학부

윤 형 석

윤형석의 이학박사 학위 논문을 인준함

2019년 8월

위 원 장:	이 규 철	(인)
부위원장:	홍 성 철	(인)
위 원:	전 헌 수	(인)
위 원:	김 창 영	(인)
위 원:	김 대 식	(인)

Abstract

In this thesis, I studied the utilization of air-filled metallic nanogaps for optical and electrochemical applications. Using atomic layer lithography, spacer-filled nanogaps are fabricated and the dielectric spacer filled in the gaps is chemically etched. Full-access into the gaps is demonstrated by measuring terahertz (THz) transmission through nanogaps and energy dispersive spectroscopy (EDS) in a scanning transmission electron microscope (STEM) setup. After etching the dielectric spacer, air-filled nanogaps are first utilized as active nano-antennas for the thermal control of optical properties of THz waves, originating from the reduction of the gap width due to thermal expansion of metals. Meanwhile, water-filled nanogaps fabricated during the chemical etching process can be served as nano-electrodes for electrochemical amplification. I fabricated the narrowest nano-electrodes with 10 nm electrode distance for redox cycling and observed amplified Faradaic current which is inversely proportional to the electrode distance. These works provide useful applications in the active thermal control of the optical responses in the nanostructures and electrochemical sensing with excellent detection sensitivity.

keywords: nanogap, active thermal control, terahertz modulation,
nano electrode, redox cycling, electrochemical amplification

student number: 2014-21380

Contents

Abstract **i**

Chapter 1 Introduction **1**

Chapter 2 Full-access into the nanogaps fabricated via a spacer-based technique **4**

2.1 Fabrication of spacer- and air-filled nanogaps via atomic layer lithography 4

2.2 Demonstration of full-etching of a dielectric spacer filled in nanogaps 9

Chapter 3 Active thermal control of THz nano-antennas **13**

3.1 Introduction: Modulation of electromagnetic waves through nanostructures combined with active materials 13

3.2 Thermal control of THz optical responses of air-filled nano-antennas . 18

3.3 Effect of a dielectric spacer on the thermal control of air-filled nano-antennas 24

3.4 Effect of the gap width on the thermal control of air-filled nano-antennas 27

3.5 Theoretical study on the thermal control of air-filled nano-antennas . . 30
3.6 Various factors related to the thermal control of air-filled nano-antennas 34
3.7 Durability of air-filled nano-antennas according to the thermal control of air-filled nano-antennas 37

Chapter 4 Electrochemical amplification in 10 nm wide nano-electrodes 40

4.1 Introduction: Electrochemical cells and redox cycling 40
4.2 Calculation of Faradaic limiting current during redox cycling 43
4.3 Fabrication of 10 nm wide nano-electrodes using modified atomic layer lithography 48
4.4 Fabrication issue: Electrostatic damage (ESD) of nano-electrodes . . . 52
4.5 Measurement of Faradaic current with 10 nm wide nano-electrodes . . 55

Chapter 5 Conclusion 60

Chapter 6 Appendix 62

6.1 Terahertz time-domain spectroscopy 62

Bibliography 64

Abstract in Korean 78

List of Figures

Figure 2.1 Schematics of the spacer-based nanogap fabrication. (a) Metal patterning by photolithography and e-beam evaporation. (b) Atomic layer deposition (ALD) of an Al_2O_3 layer. (c) Metal deposition on an Al_2O_3 layer. (d) Removal of an unnecessary metal layer by applying an adhesive tape. (e) Nanogaps formed between two metal layers. 6

Figure 2.2 Schematics of the chemical etching process. (a) As-fabricated nanogap. (b) Chemical etching of the Al_2O_3 layer by using potassium hydroxide (KOH) solution. (c) Dilution of KOH with water. (d) Fabrication of air-filled nanogap. 8

Figure 2.3 THz transmission spectra before and after wet-etching of a Al_2O_3 spacer filled in nanogaps. (a) Measured and (b) calculated THz transmission spectra. nanogaps used for the measurement and calculation are 220 nm thick, 5 nm wide and square ring-shaped with side lengths of 50 um. In calculation, the refractive index of bulk Al_2O_3 is used for optical properties of the gap material. Inconsistency of the THz resonant peaks before etching may be due to the thickness dependence of the refractive index of Al_2O_3. 10

Figure 2.4 Cross-sectional views of scanning transmission electron microscope (STEM) images of nanogaps before and after the etching process. (a-d) Energy dispersive spectroscopy (EDS) maps of Ag and K peaks before and after chemical etching, respectively. (e) An STEM image of a 5 nm wide nanogap after the etching process. 12

Figure 3.1 Schematics of the width changes of nanostructures as a result of thermal expansion. (a) Schematic of the width changes of a gold film with $\Delta T = 10$ K. (b) Plot of relative change of the gap width according to the initial gap width of the slit pattern. The relative gap width change increases as the gap width decreases. inset: schematic of the slit pattern with the gap width of w. . . 16

Figure 3.2 Nano-antennas for thermal control of THz waves. (a) Cross-sectional scanning electron microscopy (SEM) image of the nano-antennas. (b) Top-view schematic of the rectangular patterns of nano-antennas. The perimeter of the rectangular patterns is set to be resonant at THz frequency regime. 19

Figure 3.3 Measurement of THz transmission through 5 nm wide air-filled nano-antennas. (a) Normalized amplitudes of THz waves through 5 nm wide air-filled nano-antennas during heating and cooling back. Plots of the temperature-dependent (b) resonant frequencies and (c) normalized amplitudes with different maximum temperatures, T_{max}), denoted on the upper-right in each graph. 20

Figure 3.4 Top-view SEM images of the air-filled nano-antennas with different maximum temperature T_{max}. SEM images (a) before heating, (b) after heating to 150 °C and (c) after heating to 171 °C. The images are taken at room temperature after the heating process is completed. 21

Figure 3.5 THz transmission spectra of air-filled nano-antennas at 171 °C. 23

Figure 3.6 THz Transmission of the spacer-filled and air-filled nano-antennas. (a) THz transmission spectra of spacer-filled (top) and air-filled (bottom) nano-antennas. (b) Plots of the normalized amplitudes (top) and the resonant frequencies (bottom) of spacer-filled (filled circles) and air-filled (hollow circles) nano-antennas with temperature. 25

Figure 3.7 THz Transmission through a glass substrate. (a) Normalized amplitude of THz waves through a glass substrate with temperature. (b) Relative transmitted amplitudes of spacer-filled nano-antennas normalized by a glass substrate at room temperature (black line and dots) and at the same temperature where the THz transmission measurements are performed (red line and dots). Relative amplitude is almost constant with temperature after the normalization. 26

Figure 3.8 THz transmission spectra of 1.5 nm wide air-filled nano-antennas with temperature during heating and cooling back. 28

Figure 3.9 THz resonant features of 20 nm and 5 nm wide spacer-filled and air-filled nano-antennas with temperature. (a) The normalized amplitudes and (b) the resonant frequencies of 20 nm and 5 nm wide spacer-filled and air-filled nano-antennas. 29

Figure 3.10 Theoretical study on the gap width change due to thermal expansion. (a) FEM calculation by COMSOL software for the temperature-dependent gap width change. (b) Plots of the gap width (left axis) and the thickness (right axis) of air-filled nano-antennas with temperature. 31

Figure 3.11 Gap width dependence of the resonant frequency (top) and the normalized amplitude (bottom) from the experiments (dots) and the CMM calculation (thick lines). 33

Figure 3.12 Various factors related to the thermal control of the gap width. Plots of (a) thermal expansion coefficients and (b) thickness of metals versus gap width from FEM calculation. (c) Measured relative amplitudes and (d) frequencies of air-filled rectangular ring-shaped nano-antennas with side length of 10 um $\times$ 40 um and 50 um $\times$ 50 um as a function of temperature. 35

Figure 3.13 Effect of ion milling at slant angle on the performance of nano-antennas. (a) schematic of the ion milling process. (b) Relative amplitudes and frequencies of THz waves through nano-antennas with and without ion milling. 38

Figure 3.14 Normalized amplitudes (top) and resonant frequencies (bottom) of air-filled nano-antennas in several cycles of heating and cooling. 39

Figure 4.1 Schematic of an electrochemical cell. The electrochemical cell in this figure is called an electrolytic cell where a chemical reaction induced by external energy in forms of electric potential held at each electrode. 41

Figure 4.2 Schematic of an electric potential held between two electrodes filled with electrolytes. Cation and anion are relocated in order to offset an electric field across the electrochemical cell. . . . 45

Figure 4.3 Electrode distance of various electrochemical cells from the literature. The narrowest electrode distance, to the best of our knowledge, is 37 nm. 47

Figure 4.4 Fabrication schematics of side-by-side nano-electrodes. (a) Titanium/gold film deposition. (b) Vanadium patterning on Ti/Au film by photolithography and e-beam evaporation. (c) Ion milling for Au pattering (d) Atomic layer deposition of Al_2O_3 for a gap material. (e) Titanium/gold deposition to form nano-electrodes. (f) Removal of vanadium by wet etching to reveal nanogaps. (g) Electrode pattering for the fabrication of contact pads. (h) Photoresist pattering for the passivation of the upper part of the electrodes. (i) Chemical etching of Al_2O_3 for access into the nano-electrodes. 50

Figure 4.5 Optical and SEM images of a nano-electrode. (a) An optical image of a nano-electrode. nanogap is at the center of the bridge connecting the contact pads. (b) A cross-sectional SEM image of the nano-electrode. the electrode is 100 nm thick, 20 um long and 10 nm wide. (c) and (d) top-view images of the nano-electrode. 51

Figure 4.6 SEM images of a nano-electrode before (a) and after (b) electrostatic damage. Once damaged, the gap width of the nano-electrode is broadened from 10 nm to several microns. 53

Figure 4.7 Schematic of the nano-electrode pattern to prevent ESD. . . . 54

Figure 4.8 Schematic of experimental setup for cyclic voltammetry. . . . 55

Figure 4.9 Schematics of preparation of nano-electrodes with redox species filled. 56

Figure 4.10 Cyclic voltammogram of redox cycling. 57

Figure 4.11 Calculated (line) and experimental (star) Faradaic limiting current. 58

Figure 4.12 Plots of Faradaic limiting currents among [85], [68] and this work. Electrode area and ion concentration in these works are normalized to correct the same experimental condition. 59

Figure 6.1 Schematic of a THz time-domain spectroscopy setup. 63

List of Tables

Table 3.1 Coefficients of linear thermal expansion of various materials. . 15

Chapter 1

Introduction

Nano-optics has recently been one of the most important research fields in optics for its versatile modulations of electromagnetic waves with metallic nanostructures. In particular, when electromagnetic waves are transmitted through sub-wavelength hole array, transmission at the specific wavelength corresponding to the period of the array is abnormally increased. This phenomenon is known as extraordinary transmission, resulting from the coupling of electromagnetic waves with surface plasmons (SPs) over visible and near-infrared (NIR) frequencies [1]. The SP-mediated phenomenon is widely used for various optical applications such as surface-enhanced Raman spectroscopy (SERS) [2–9], metamaterials and optical antennas [10–14].

Meanwhile, terahertz (THz) frequency (10^{12} Hz) is an intermediate frequency between electronics (1 GHz) and optics (100 THz), at which photon energy is about a few meV and lies on inter-molecular interactions applicable for various phenomena [12, 15–19]. Generally, it is difficult to excite SPs at THz frequency range because

of its low photon energy and negligible coupling of THz waves with plasmonic surface. However, Lee et al [20] achieved near-unity transmission of THz waves through sub-wavelength hole array, which is similar to the extraordinary transmission at visible wavelength. The perfect transmission at THz frequency can be explained by capacitor model considering single slot antenna as a current source [10]. One of the important result is that when THz waves go through the metallic gaps, the electric field in the gap is extremely amplified and is inversely increased with the gap width [10]. Therefore, it becomes crucial to reduce the gap width for higher electric field enhancement and thus further optical applications. The reduction of the gap width, to some extent, can be achieved thanks to the conventional fabrication techniques such as focused ion beam (FIB) [21] or electron-beam (e-beam) lithography [22] for the fabrication of the nanostuructures resonant at sub-millimeter wavelength. However, these fabrication techniques are time-consuming and not appropriate to realize narrow nanogaps with the gap width below tens of nanometers.

To realize sub-10 nm wide nanogaps, a dielectric spacer-based fabrication technique is newly developed by combining photolithography and atomic layer deposition, which is called atomic layer lithography [23]. The atomic layer lithography technique overcomes the spatial limits via wafer-scale fabrication by photolithography and sensitive control of the gap width as narrow as 1 nm by ALD. The optical properties of the nanogaps fabricated by the spacer-based technique have been characterized at visible-to-NIR [23–26], THz [23, 27–36] and even gigahertz [37] frequencies. The nanogaps

also realize THz quantum plasmonics [28, 30, 36], a vanadium dioxide metamaterial [38], near-field lithography [39], THz nano-probing [40] and ultrathin film sensing [41].

However, these applications have no choice but to utilize the fringe field from the gap, even though electric field inside the gap is much higher than that near the gap. This is because the access into the gap is not allowed due to the dielectric spacer filled in the gaps, limiting broad applications of the nanogaps. In other words, it is required to access into the gap by removing the gap material for further applications.

In this thesis, I fabricate air-filled nanogaps by etching the dielectric spacer filled in the nanogaps, and utilize them as nano-antennas for thermal control of THz waves and as nano-electrodes for Faradaic current amplification in electrochemistry.

Chapter 2

Full-access into the nanogaps fabricated via a spacer-based technique

2.1 Fabrication of spacer- and air-filled nanogaps via atomic layer lithography

Schematics of nanogap fabrication via atomic layer lithography [23] are shown in figure 2.1. On pre-cleaned glass substrates (Pyrex), hexamethyldisilazane (HMDS) and AZ 5214E image reversal photoresist are spin-coated at 4000 rpm for 60 seconds and baked at 90 °C for 60 seconds, respectively. Ultraviolet (UV) light (wavelength ranging from 350 nm to 450 nm and beam intensity of 25 mW/cm^2 at the center wavelength of 365 nm) is exposed on the substrates for 6 seconds (Midas mask aligner), and post-baking process is made at 120 °C for 120 seconds. After flood exposure with UV light for 40 seconds, development is performed by using AZ 500 MIF developer for

40 seconds and cleaned in distilled water for more than 1 minute. The photolithography condition can be slightly different depending on substrate types, pattern sizes and ambient humidity and temperature. Chromium and silver are deposited on the pre-patterned glass substrates by an electron-beam evaporator (Korea Vacuum Tech.) with deposition rate of 1 Å/s. Here chromium acts as an adhesion layer between noble metal and the substrate. Remaining photoresist after metal deposition is lifted off by ultrasonication in acetone for a few seconds (figure 2.1 (a)) and the patterned metallic steuctures are cleaned by using isopropyl alcohol and dried with nitrogen blow. A dielectric spacer, Al_2O_3 is conformally coated along the patterned metallic structures by ALD (figure 2.1 (b)). The dielectric spacer determines the width of nanogaps. After silver layer is deposited again onto the structures (figure 2.1 (c)), a part of metal layers piled up on the bottom layer is lifted off by applying an adhesive tape to flatten the surface of metallic structures and to reveal nanogaps (figure 2.1 (d) and (e)). After peeling off unnecessary metals, the remaining silver debris along the gaps are removed by Ar ion beam milling (Korea Vacuum Tech) at slant angle of 80° for 5 minutes.

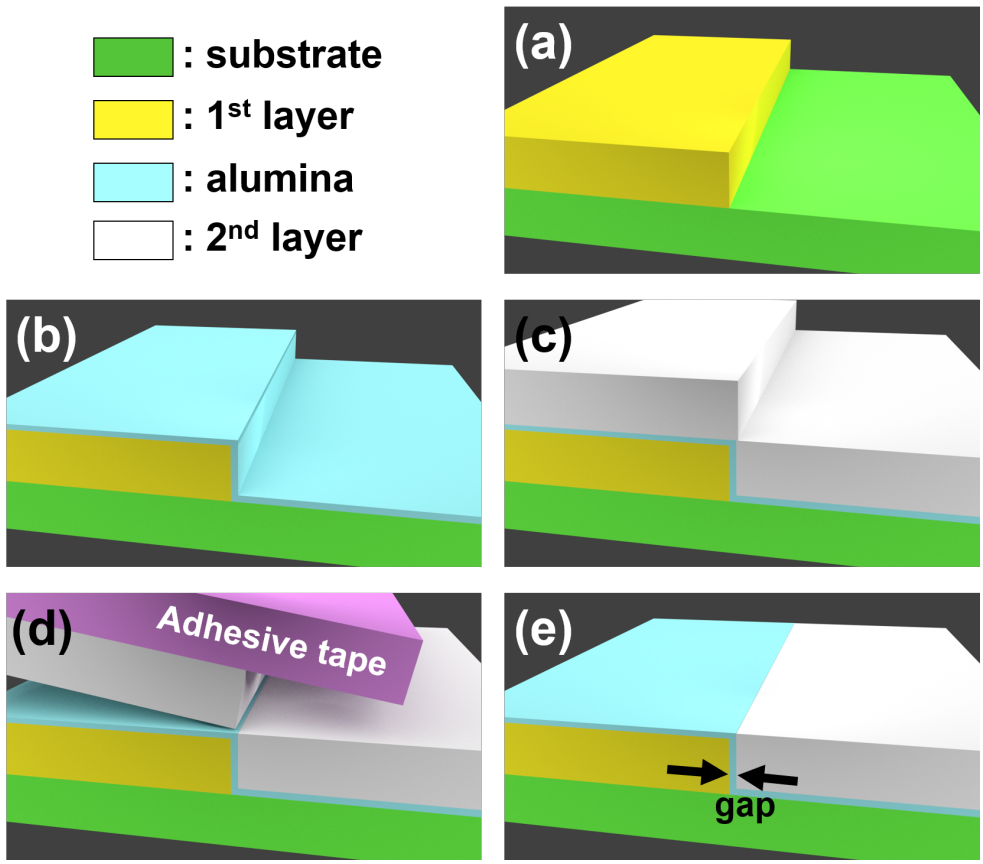

Figure 2.1: Schematics of the spacer-based nanogap fabrication. (a) Metal patterning by photolithography and e-beam evaporation. (b) Atomic layer deposition (ALD) of an Al_2O_3 layer. (c) Metal deposition on an Al_2O_3 layer. (d) Removal of an unnecessary metal layer by applying an adhesive tape. (e) Nanogaps formed between two metal layers.

To fabricate air-filled nanogaps, dielectric spacer filled in the gap should be etched. Before etching dielectric spacer filled in the gap, it is required to check if an etchant can permeate into the metallic gap because height-to-width ratio of the ordinary nanogap (200 nm thick and 5 nm wide) is as high as 40:1. And the nanostructures with high aspect ratio are generally used for hydrophobic surface [42]. Thus, it might be hard to fully fill an etchant into the gaps. Unlike common hydrophobic nanostructures, however, the nanogaps here are fully filled with a dielectric spacer, and the etchant can occupy the inside of gaps where the dielectric spacer was filled, demonstrating full-etching of the dielectric spacer filled in the gaps. Al_2O_3 spacer filled in the gaps is chemically etched out in 1 M potassium hydroxide (KOH) solution for 1 minute and kept in deionized water for more than 30 minutes. After drying water with nitrogen blow, air-filled nanogaps are completely fabricated as shown in 2.2. The air-filled nanogaps are easy to get damaged upon pressure on the gap, as the spacer sustaining the gaps is removed.

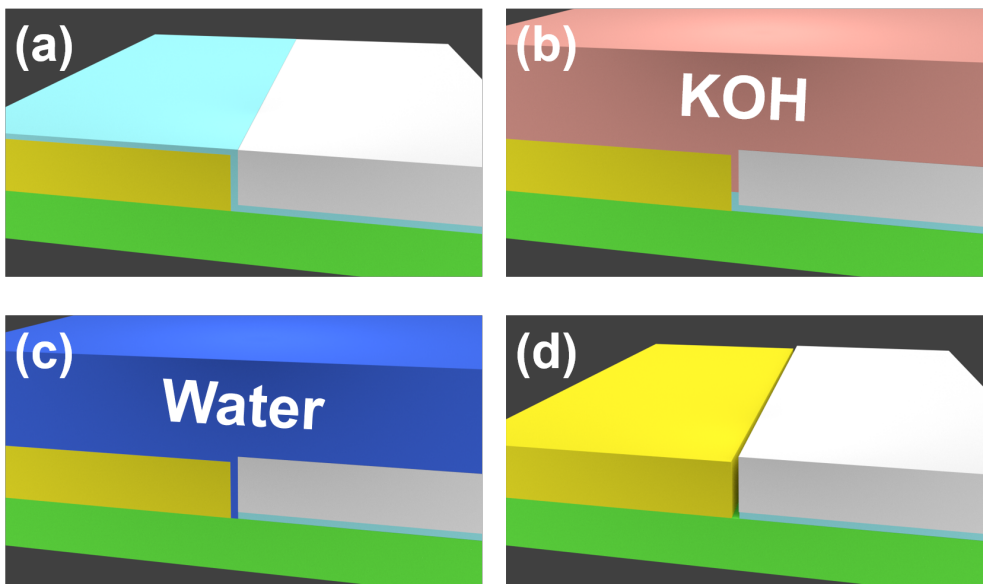

Figure 2.2: Schematics of the chemical etching process. (a) As-fabricated nanogap. (b) Chemical etching of the Al_2O_3 layer by using potassium hydroxide (KOH) solution. (c) Dilution of KOH with water. (d) Fabrication of air-filled nanogap.

2.2 Demonstration of full-etching of a dielectric spacer filled in nanogaps

Full-access into the air-filled nanogaps can be demonstrated optically by comparing THz transmission spectra before and after the etching process. The resonant features of THz nanogaps highly depend on dielectric environment near the gaps if the gap is small enough to support gap plasmons which is a coupling of surface plasmons on each side of a metal-dielectric-metal interface [34]. Thus, the change in effective dielectric constant after etching the gap material leads to the larger change in the resonant features, and the shift of the resonant peaks can be an evidence of full-etching of the gap material.

Figure 2.2 represents THz transmission spectra of 220 nm thick, 5 nm wide and square-shaped nanogaps before (black line) and after (red line) etching the gap material. THz transmitted amplitudes are measured by THz time-domain spectroscopy (THz-TDS) (See appendix). After chemical etching, both experimental and simulated spectra show in figure 2.2 the similar trend that the resonant frequencies are blue-shifted and the normalized amplitudes are increased. It is surprising that the nanogaps still sustain the structures after the gap material is etched out, Considering extreme height-to-width ratio of about 40:1.

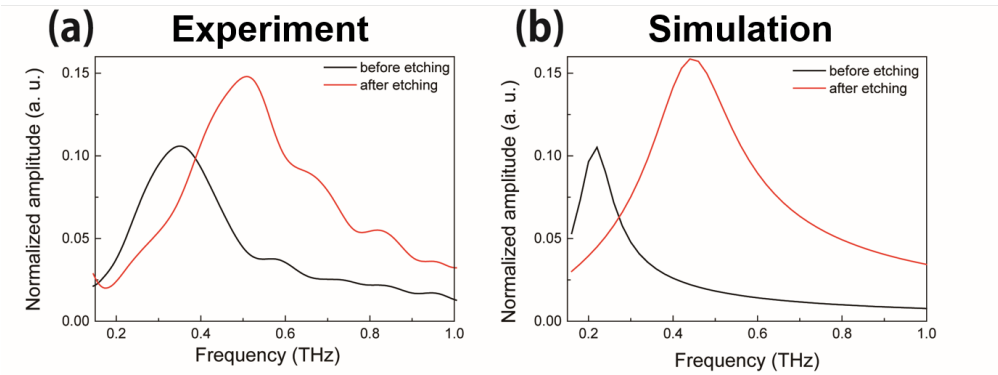

Figure 2.3: THz transmission spectra before and after wet-etching of a Al_2O_3 spacer filled in nanogaps. (a) Measured and (b) calculated THz transmission spectra. nanogaps used for the measurement and calculation are 220 nm thick, 5 nm wide and square ring-shaped with side lengths of 50 um. In calculation, the refractive index of bulk Al_2O_3 is used for optical properties of the gap material. Inconsistency of the THz resonant peaks before etching may be due to the thickness dependence of the refractive index of Al_2O_3.

Meanwhile, energy dispersive spectroscopy (EDS) is a powerful tool to analysis spatial distribution of specific elements composed in nanostructures. To directly confirm that the gap material filled in the gaps is fully etched out, EDS in a scanning transmission electron microscope (STEM) setup is used to measure the energy spectra of transmitted electrons from aluminum included in Al_2O_3 and to map K-level atomic transition of aluminum.

Figure 2.4 shows cross-sectional EDS maps of K peak of silver and aluminum from nanogaps used in the THz transmission measurements. In the EDS maps in figure 2.4 (a) and (b), Ag K peaks can be seen except in the gap area before and after etching process, implying the nanogaps are not collapsed after the etching process. In contrast, Al K peaks along the gap in figure 2.4 (c) disappear after etching process as in figure

2.4. The EDS maps confirm the full-etching of the gap material. Al K peaks shown in the bottom of images originate from the substrate (sapphire, Al_2O_3). From cross-sectional STEM image in figure 2.4 (e), the nanogaps do not collapse and sustain its geometrical structure after etching.

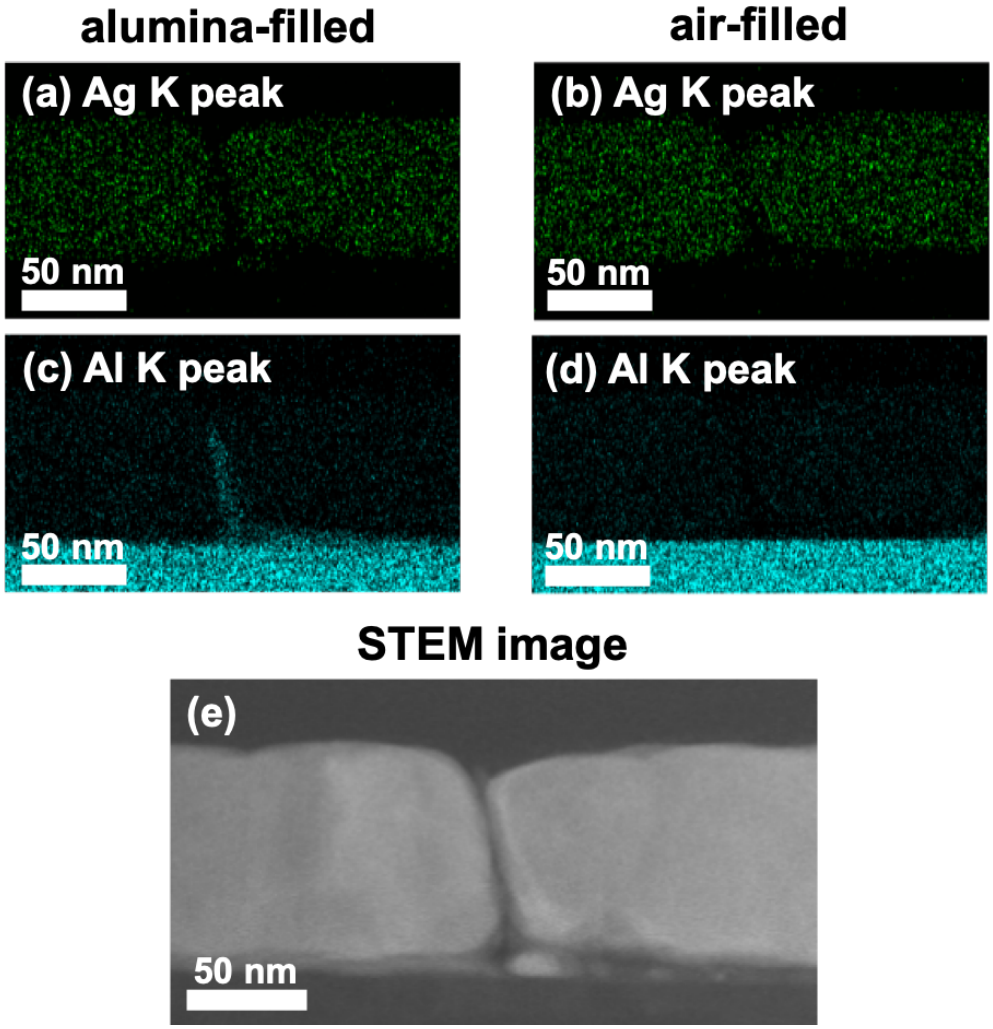

Figure 2.4: Cross-sectional views of scanning transmission electron microscope (STEM) images of nanogaps before and after the etching process. (a-d) Energy dispersive spectroscopy (EDS) maps of Ag and K peaks before and after chemical etching, respectively. (e) An STEM image of a 5 nm wide nanogap after the etching process.

Chapter 3

Active thermal control of THz nano-antennas

3.1 Introduction: Modulation of electromagnetic waves through nanostructures combined with active materials

Hotspot, where electromagnetic waves are extremely confined into sub-wavelength metallic nanostructures, has been widely studied due to the colossal electric field enhancement and optical nonlinear phenomena [1, 10, 23, 28, 43, 44]. Increasing demands for higher electric field enhancement and desired nanostructures lead to the integration of metallic nanostructures with various active materials to modulate optical properties of electromagnetic waves [13, 22, 45–47]. In particular, transmitted amplitudes of terahertz waves are well modulated under a gate voltage by fabricating nanostructures on single graphene layer [48] or a semiconductor [49]. On the other hand, by patterning nanodisks on a polymer-based flexible substrate, it is possible to

modulate optical properties at visible wavelength, by applying lateral stress across the substrate [50]. Recently, vanadium dioxide, which shows an insulator-to-metal phase transition occurring at around 68 °C, has been widely investigated for a thermal modulator for various applications, such as anomalous transition properties [38], thermal memory [51], thermal rectification with higher electrical performance [52] and a hybrid thermal diode integrating metals and superconductors [53].

For the thermal control of optical and electrical properties of metallic nanostructures, it is required to minimize thermal deformation or melting of metals under moderate temperature changes. Particularly, as a melting point of metals at nanoscale is decreased compared to that of bulk ones, operating temperature is highly limited [54]. Thus, the metallic nanostructures in shape of a sharp tip, a nanoparticle, a bowtie antenna and a thin sheer can be easily melt, implying that thermal deformation is detrimental for metallic nanostructrue. Even though several studies overcome the structural limit at nanoscale by conformally coating dielectrics on metallic nanostructures using ALD [55] or by using refractory materials [56], thermal deformation is still inevitable in order to realize thermally-controlled nano-optic devices.

Meanwhile, thermal deformation does not always have a negative effect on the thermal control of nano-devices; rather, in a moderate temperature range where melting of metals is negligible, there is a possibility to induce the structural change of the nanostructures using well-known thermal expansion phenomenon. In linear thermal expansion regime, relative length change of a material at an elevated temperature is

expressed as

$$\Delta L/L = \alpha \Delta T \tag{3.1}$$

where L is a length of a material, α is a linear thermal expansion coefficient, and T is temperature. The change in length of a material is proportional to the thermal expansion coefficient, an original length of a material and a change in temperature, all of which should be considered for a enough change in a structural change of the nanostructures.

Material	Linear thermal expansion coefficient $(10^{-6}K^{-1})$
Aluminum	21 - 24
Chromium	6 - 7
Copper	16 - 16.7
Gold	14.2
Silver	19
Glass	4
Silicon	3 - 5

Table 3.1: Coefficients of linear thermal expansion of various materials.

Here, I explored a possibility to utilize thermal expansion for thermal control of nanostructures. Thermal expansion coefficients of widely used metals are of order of $10^{-5}\ K^{-1}$ as shown in table 3.1 [57]. The length change of thin gold film in 50 µm $\times$ 50 µm rectangular shape, for example, is about 0.007 µm if ΔT = 10 K as shown in figure 3.1 (a). The length change is negligible compared to the pattern size and hard to observe with electromagnetic waves with wavelength resonant at the pattern size.

Meanwhile, to increase the amount of length change, increasing temperature much more can be a alternative solution, but it results in the melting of the nanosutructures even at the temperature where bulk materials would have not melt. In other words, changes in the optical response of nanostructures due to thermal expansion are negligible in practical temperature ranges.

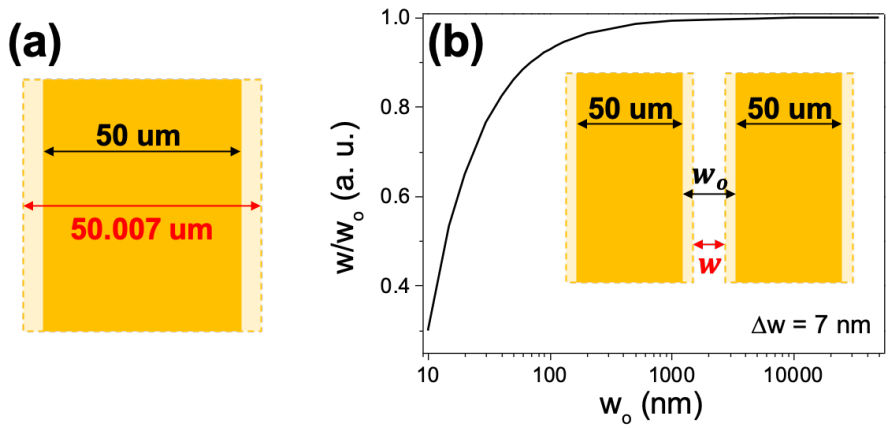

Figure 3.1: Schematics of the width changes of nanostructures as a result of thermal expansion. (a) Schematic of the width changes of a gold film with ΔT = 10 K. (b) Plot of relative change of the gap width according to the initial gap width of the slit pattern. The relative gap width change increases as the gap width decreases. inset: schematic of the slit pattern with the gap width of w.

However, if the gap width between the patterns becomes reduced compared to the pattern size, as in figure 3.1 (b), the relative gap width change (w/w_0) becomes larger as the original gap width (w) becomes smaller. Thus, the micrometer-scaled patterns with the nanometer-scaled gap width can be used for the detection of the gap width change and the thermal control of optical responses of the nanogaps. In this chapter,

I realized active thermal control of transmitted THz waves through air-filled nano-antennas, which mainly results from the change in the gap width, by means of thermal expansion.

3.2 Thermal control of THz optical responses of air-filled nano-antennas

Air-filled nanogaps as nano-antennas for thermal control are fabricated in the same way as described in chapter 2. The air-filled nano-antennas are 220 nm thick, 5 nm wide, and square ring-shaped with side lengths of 50 µm. The spacing between square patterns is 50 µm in each direction, as in figure 3.2. I measured THz field amplitudes transmitted through 5 nm wide air-filled nano-antennas at different temperatures using a THz-TDS setup with heating plate attached on an aperture for temperature modulation. To obtain normalized amplitudes of THz waves, THz field amplitudes through nano-antennas at each temperature are divided by those through a glass substrate at room temperature.

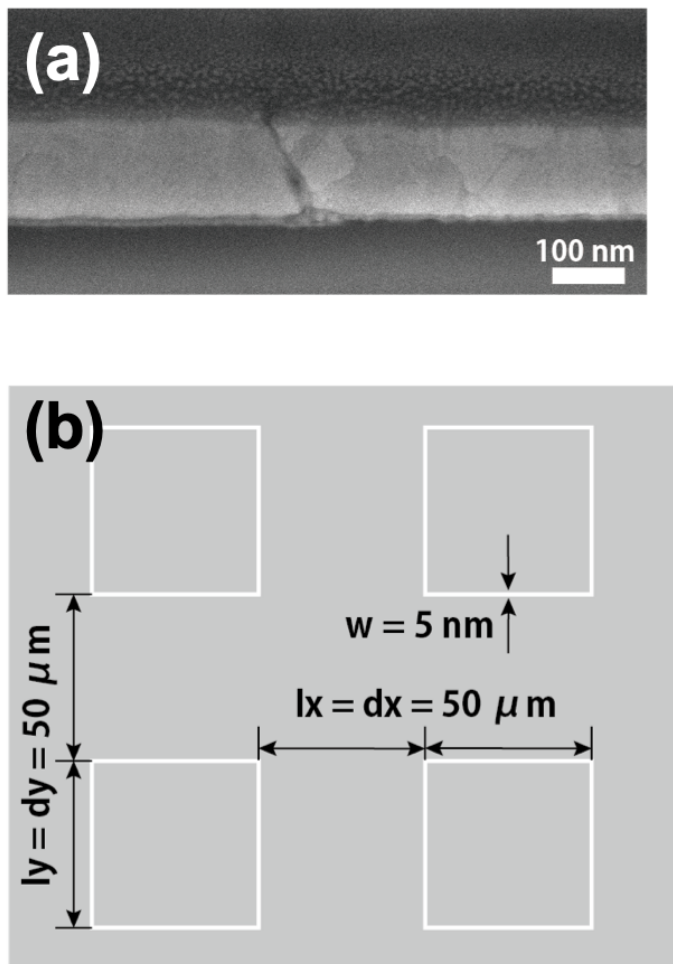

Figure 3.2: Nano-antennas for thermal control of THz waves. (a) Cross-sectional scanning electron microscopy (SEM) image of the nano-antennas. (b) Top-view schematic of the rectangular patterns of nano-antennas. The perimeter of the rectangular patterns is set to be resonant at THz frequency regime.

THz transmission spectra of nano-antennas during heating and cooling back are plotted in figure 3.3 (a). At room temperature, the normalized amplitude and the resonant frequency are 0.15 and 0.45 THz, respectively. As temperature increases from 29.5 °C to 149.5 °C, the normalized amplitude decreases from 0.15 to 0.12 (by 20%) and the resonant frequency is red-shifted from 0.45 THz to 0.35 THz (by 22%). Meanwhile, it is noteworthy that the resonant features are fully recovered to the initial values after cooling back, meaning that the spectral changes may originate from the reversible structural changes, not from permanent damage on the nano-antennas due to melting of metals. Here the changes are attributed to the gap width change resulting from thermal expansion of metals, which is discussed later in detail.

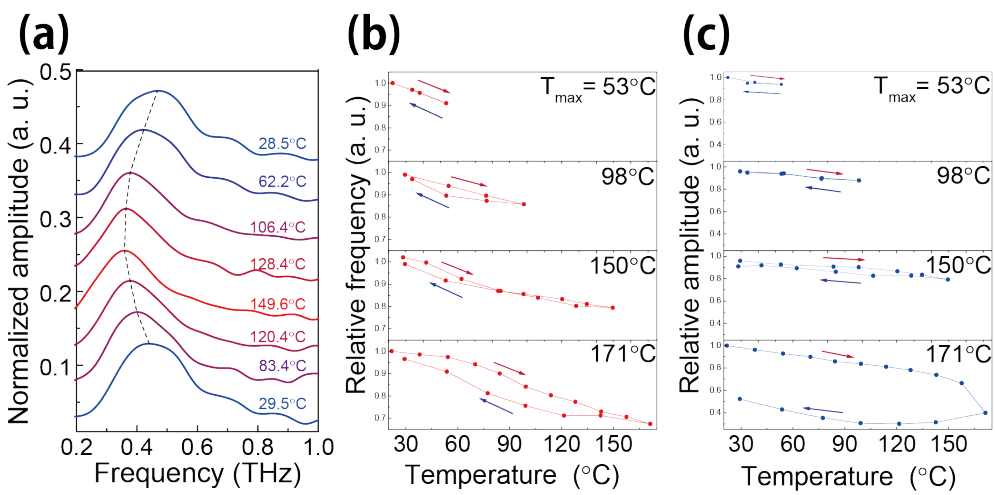

Figure 3.3: Measurement of THz transmission through 5 nm wide air-filled nano-antennas. (a) Normalized amplitudes of THz waves through 5 nm wide air-filled nano-antennas during heating and cooling back. Plots of the temperature-dependent (b) resonant frequencies and (c) normalized amplitudes with different maximum temperatures, T_{max}), denoted on the upper-right in each graph.

For thorough investigations on the resonant features, the normalized amplitude and the resonant frequency with temperature are plotted in figure 3.3 (b) and 3.3 (c), respectively. THz transmission measurements in a cycle of heating and cooling back are performed several times with different maximum temperature, T_{max}, denoted on the upper-right in each graph in figure 3.3 (b) and (c). The resonant features are shown to be changed monotonically and the plots during heating and cooling are well overlapped with T_{max} below 150 °C. That is, the changes in the optical properties of the nano-antennas are reversible within a moderate temperature range. This can be seen in figure 3.4 (a) and (b), top-view SEM images of nano-antennas with different maximum temperatures imply that the gaps become smooth after heating the nano-antennas, which can be regarded as an annealing process. In spite of the structural changes, the optical properties of the nano-antennas are still unchanged even after the heating process is completed with a moderate temperature range.

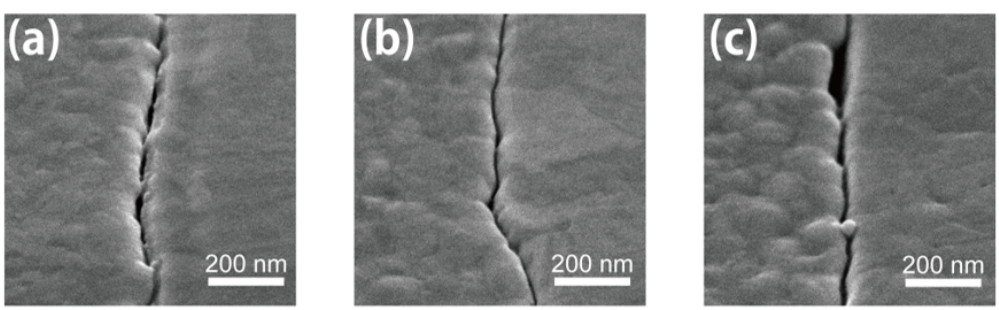

Figure 3.4: Top-view SEM images of the air-filled nano-antennas with different maximum temperature T_{max}. SEM images (a) before heating, (b) after heating to 150 °C and (c) after heating to 171 °C. The images are taken at room temperature after the heating process is completed.

When T_{max} exceeds 150 °C, however, the normalized amplitude is rapidly reduced and cannot be recovered to the initial value even after cooling back, as shown in the bottom graph of figure 3.3 (c). The decrease in the normalized amplitude implies that the damage on the nano-antennas results from the melting of the sidewalls consisting of the nano-antennas at T_{max} = 171 °C. The traces of the dmage at the critical temperature, T_{max} = 171 °C, can be found in figure 3.4 (c) where nano-antennas are broadened or connected. Figure 3.5 shows that the normalized amplitude at the critical temperature decreases in real time, demonstrating that the deformation of nano-antennas occurs. Once damaged at the critical temperature, the nano-antennas cannot function as THz resonators, leading the decrease in the normalized amplitude even after cooling back. In contrast to the rapid drop in the normalized amplitudes, the resonant frequency is recovered after cooling back. This can be interpreted that, if some nano-antenna patterns do not melt at the critical temperature, they can act as THz nano-resonators.

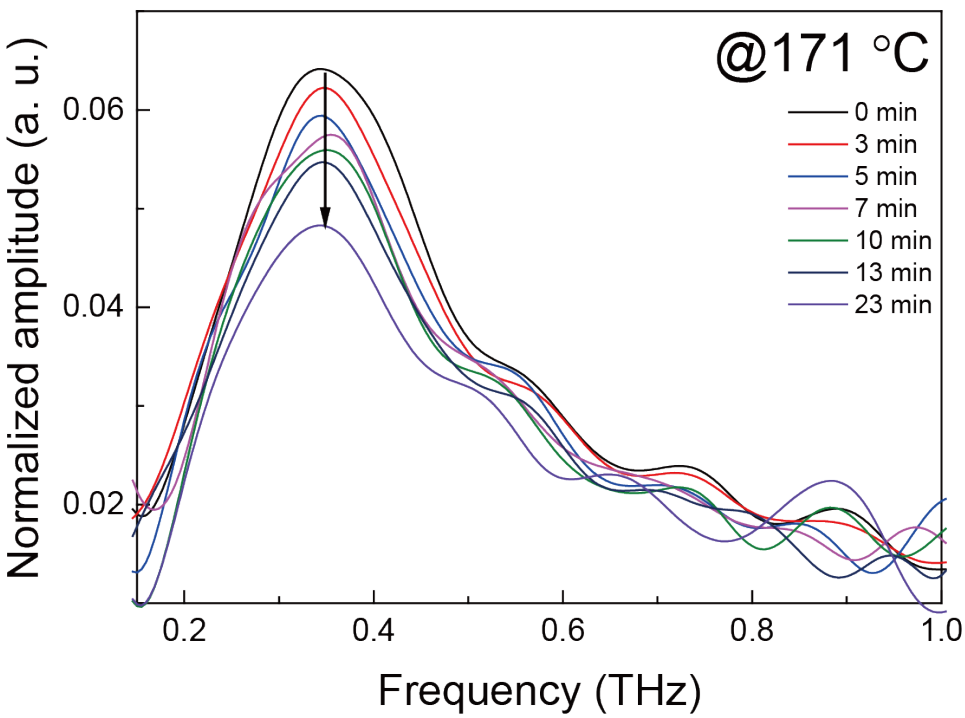

Figure 3.5: THz transmission spectra of air-filled nano-antennas at 171 °C.

3.3 Effect of a dielectric spacer on the thermal control of air-filled nano-antennas

To confirm that the change in the THz resonant features originate from the change in the gap width, it is required to check if the gap width is really changed with temperature. If nano-antennas are filled with a dielectric spacer, the gaps could not be changed. As a control experiment, I compare in figure 3.6 THz transmission spectra of air-filled and spacer-filled nano-antennas. During heating, the normalized amplitude decreases and the resonant frequency is red-shifted monotonically in both cases, as shown in figure 3.6 (a). However, there are some differences between two cases.

The changes in the resonant features of spacer-filled nano-antennas may result from slight decrease in THz transmission through a glass substrate, as shown in figure 3.7 (a). The normalized amplitude of spacer-filled nano-antennas is shown to be constant if THz electric field amplitude through nano-antennas is normalized by that through a substrate at the same temperature where THz transmission measurement of nano-antennas is conducted, as in figure 3.7 (b). The decrease in the THz transmitted amplitude implies that the refractive index of a substrate is changed, leading to the change in the resonant frequency which is sensitive to the refractive index of surrounding medium. That is, the changes in the normalized amplitude and the resonant frequency of spacer-filled nano-antennas may originate from the change in the optical properties of a glass substrate with temperature.

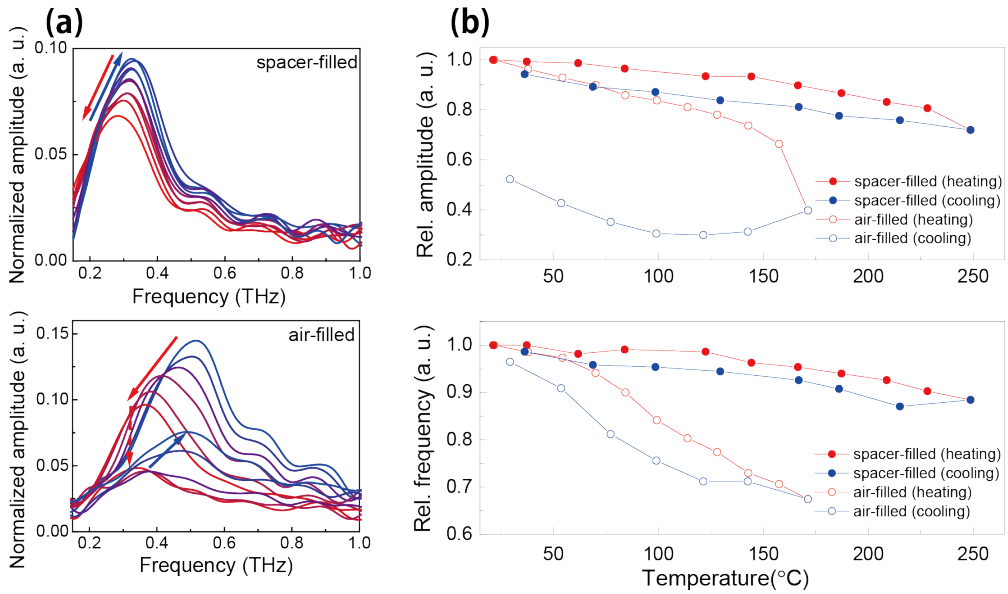

Figure 3.6: THz Transmission of the spacer-filled and air-filled nano-antennas. (a) THz transmission spectra of spacer-filled (top) and air-filled (bottom) nano-antennas. (b) Plots of the normalized amplitudes (top) and the resonant frequencies (bottom) of spacer-filled (filled circles) and air-filled (hollow circles) nano-antennas with temperature.

Secondly, while air-filled nano-antennas get damaged at T_{max} = 171 °C as in figure 3.6 (b), spacer-filled nano-antennas are not damaged even at T_{max} = 250 °C because Al_2O_3 spacer can be used as a protection layer to prevent abrupt melting [55]. This results can be used for the improvement in the operating temperature of the thermal control of air-filled nano-antennas, for example, by coating dielectric layer after etching a gap material. Lastly, air-filled nano-antennas result in more significant changes in the resonant features compared to spacer-filled ones, verifying that dielectric spacer prevents metals from expanding during heating in case of spacer-filled slot antennas. The thermal control of air-filled nano-antennas can most likely result from thermal expansion of metals affecting the gap width change.

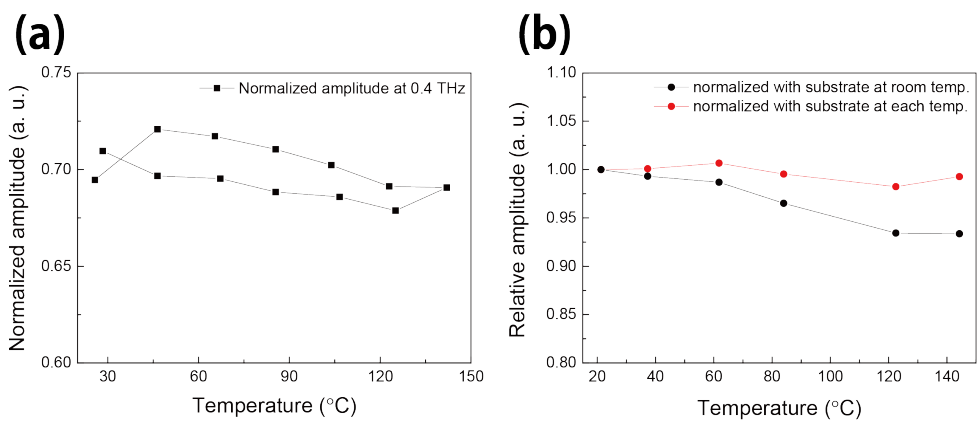

Figure 3.7: THz Transmission through a glass substrate. (a) Normalized amplitude of THz waves through a glass substrate with temperature. (b) Relative transmitted amplitudes of spacer-filled nano-antennas normalized by a glass substrate at room temperature (black line and dots) and at the same temperature where the THz transmission measurements are performed (red line and dots). Relative amplitude is almost constant with temperature after the normalization.

3.4 Effect of the gap width on the thermal control of air-filled nano-antennas

As thermal expansion is a linear process, the amount of the gap width change of the nano-antennas with different gap widths should be same, as discussed in figure 3.1 (b). That is, THz resonant features of nano-antennas with different gap widths show different behavior. To investigate the effect of the gap width on thermal control of THz resonant features, I compare THz transmission spectra of 1.5 nm, 5 nm, and 20 nm wide nano-antennas.

Figure 3.8 (a) shows THz transmission measurement of 1.5 nm wide air-filled nano-antennas. Compared to 5 nm wide nano-antennas permanently damaged at 171 °C, 1.5 nm wide nano-antennas are shown to drag down the critical temperature from 171 °C to less than 110 °C, thus limiting the operating temperature range of the nano-antennas. Moreover, while the normalized amplitude decreases, the resonant frequency is not shifted because the gap width is too narrow to show the spectral changes. THz normalized amplitude does not bring back to the initial value even after cooling back, suggesting that the sidewalls of air-filled nano-antennas are fully stuck together, and the nano-antennas are deformed to the thin metal film. I also measure THz transmission of 20 nm wide air-filled nano-antennas in figure 3.8 (b). The amount of change is very small compared to that of 1.5 nm wide nano-antennas.

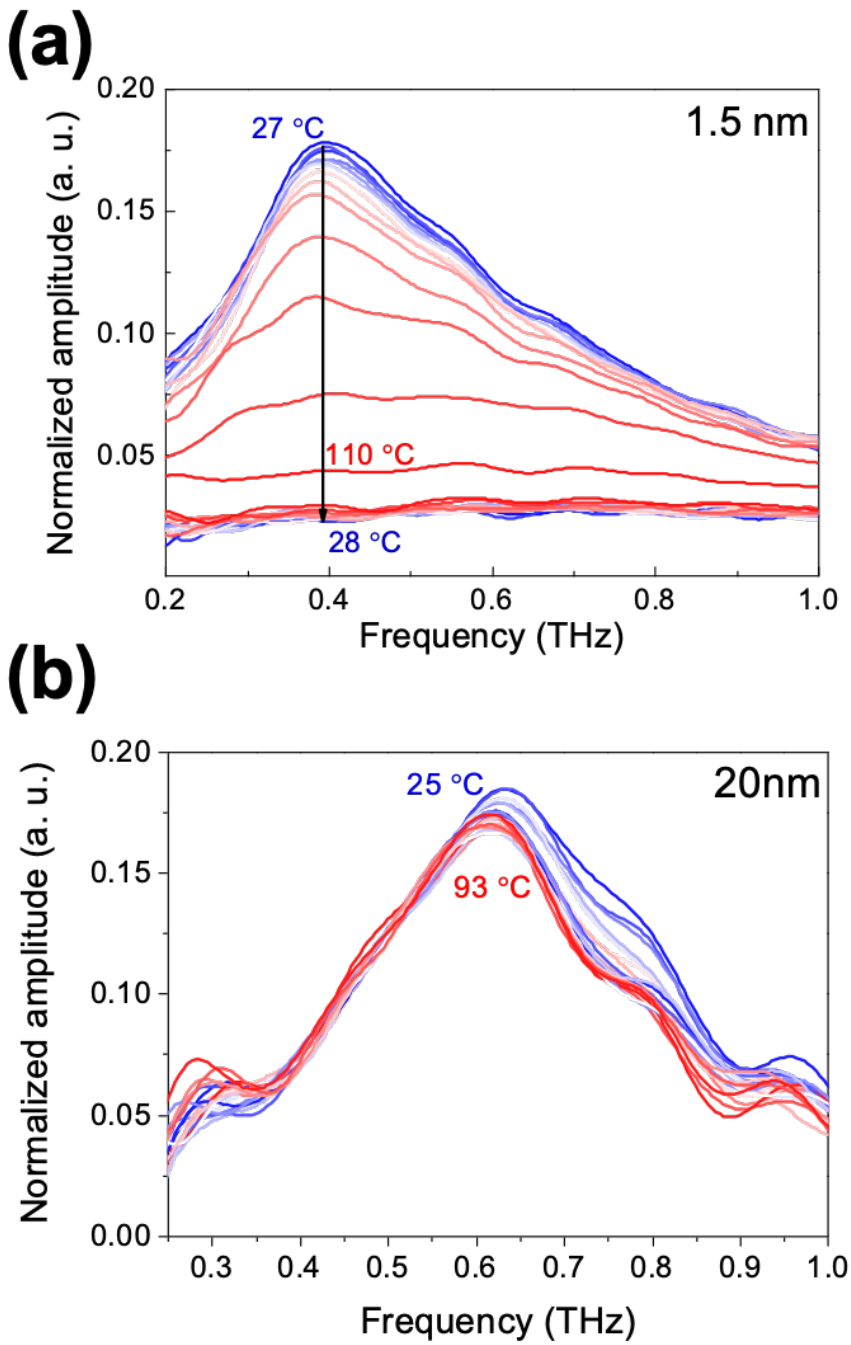

Figure 3.8: THz transmission spectra of 1.5 nm wide air-filled nano-antennas with temperature during heating and cooling back.

I also compared relative frequency and amplitude of 5 nm and 20 nm wide air-filled nano-antennas with temperature. It is shown that the amount of changes in the resonant features of 20 nm wide air-filled nano-antennas are slightly smaller than those of spacer-filled ones. However, the spectral changes are still very small compared to those of 5 nm wide air-filled nano-antennas, which can be explained by thermal expansion as mentioned above. It is noteworthy that there is a trade-off between the operating temperature range and modulation depth of the resonant features. And the use of nano-antennas with appropriate gap width is important for the desired performance as thermally-controlled nano-optic devices.

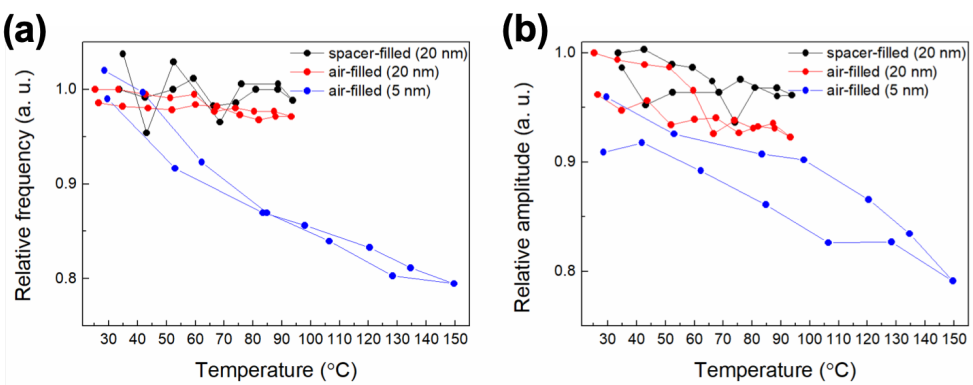

Figure 3.9: THz resonant features of 20 nm and 5 nm wide spacer-filled and air-filled nano-antennas with temperature. (a) The normalized amplitudes and (b) the resonant frequencies of 20 nm and 5 nm wide spacer-filled and air-filled nano-antennas.

3.5 Theoretical study on the thermal control of air-filled nano-antennas

For thorough investigation, I discuss theoretical study on the effect of thermal expansion on the control of the THz waves through air-filled nano-antennas. First, finite element method (FEM) calculation is performed by using COMSOL software to predict the gap width at the specific temperature, because the gap width at the elevated temperature is hard to directly measure. During heating from 25 to 190 °C, the gap width of the nano-antennas is expected to decrease from 5 nm to 2 nm as a result of thermal expansion of metals, as shown in figure 3.10 (a). I display in figure 3.10 (b) the width and thickness changes of the nano-antennas with temperature, and define the narrowest gap distance between sidewalls as the gap width at each temperature [29]. It in noted that the width and thickness of the nano-antennas linearly increase during heating because thermal expansion is a linear process in moderate temperature ranges. While the gap width of the nano-antennas shrinks by 40% during heating from 25 °C to 190 °C, the thickness of nano-antennas remains nearly constant and thus has a negligible effect on the spectral changes in THz transmitted amplitude.

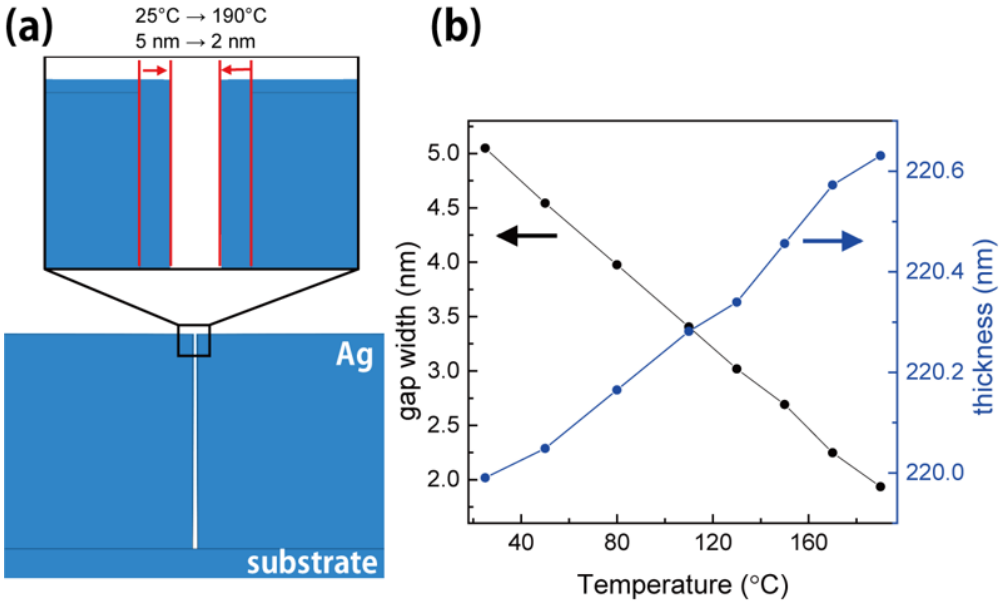

Figure 3.10: Theoretical study on the gap width change due to thermal expansion. (a) FEM calculation by COMSOL software for the temperature-dependent gap width change. (b) Plots of the gap width (left axis) and the thickness (right axis) of air-filled nano-antennas with temperature.

Combining the gap width speculated from the FEM calculation in figure 3.10 and the THz resonant features measured in the experiments in figure 3.3, the normalized amplitude and the resonant frequency as a function of the gap width are plotted in figure 3.11 (dots), respectively. We also conduct Coupled-Mode Method (CMM) calculation to theoretically obtain the THz transmission spectra of the air-filled nano-antennas with different gap widths. The CMM calculation is well-known theoretical approach of Maxwell equation and modal expansion to obtain the electromagnetic field distribution around metallic structures [43], and here I conduct the calculation performed by Kim [34].

The resonant frequency and the normalized amplitude are plotted in 3.11 (thick line). Even though the normalized amplitude in the experimental data slightly deviates from that in the calculation, both follow the same tendency where the normalized amplitude is decreased as the gap width is reduced. The deviation in the normalized amplitude might be due to the fabrication error. The resonant frequency with respect to the gap width is consistent in the experiment and the calculation. Overall, the results strongly indicate that decrease in the gap width is due to thermal expansion of metals, and is responsible for the observed changes in the resonant features.

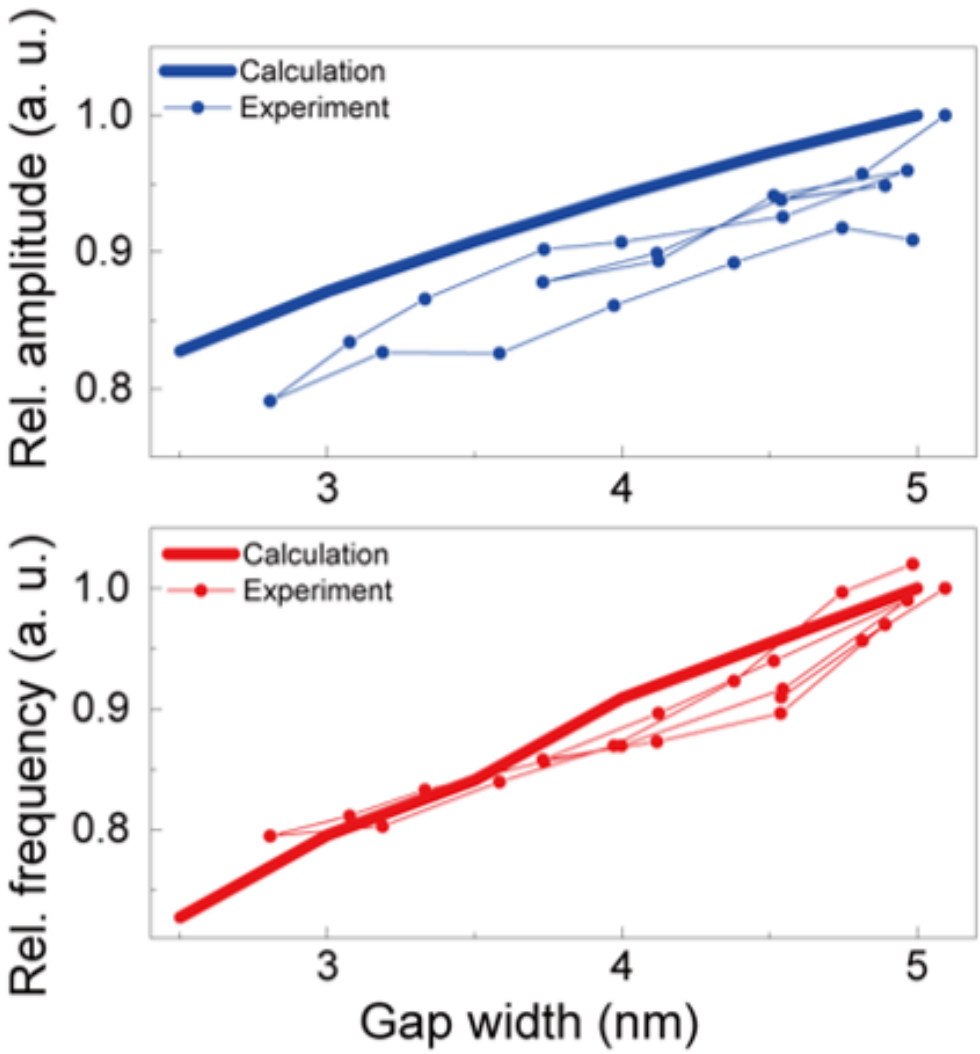

Figure 3.11: Gap width dependence of the resonant frequency (top) and the normalized amplitude (bottom) from the experiments (dots) and the CMM calculation (thick lines).

3.6 Various factors related to the thermal control of air-filled nano-antennas

There are various factors affecting the thermal control, and it is of importance to consider the factors in order to fully characterize the properties of the air-filled nano-antennas for the active thermal control. I categorize the factors into four varieties: an adhesion layer, the thermal coefficient of metals and substrates, the thickness of metals, and the size of metal patterns.

First, chromium adhesive layer attached on the first metallic patterns might affect the spectral changes with temperature, considering that chromium/silver layer and silver layer can show different structural changes. However, the adhesive layer is usually less than 3 nm thick, and forms like island structures. Thus, the adhesive layer is hardly considered as another metallic layer attached on the substrate, which might have a negligible effect on the thermal control.

Second, to characterize the effect of thermal expansion coefficient on the thermal control, I theoretically substitute metal and substrate materials with the other materials of different thermal expansion coefficient, performed by FEM calculation used above. I plot in figure 3.12 (a) the gap width of the 5 nm wide silver, gold and copper nano-antennas. As thermal expansion is a linear process, it is not surprising that the gap width changes at the elevated temperature of 170 °C are linearly dependent on the thermal expansion coefficient. Meanwhile, for substrate materials, the linear ther-

mal expansion coefficients of widely used substrates in THz regime are 4 for Pyrex glass, 5.3 for sapphire, and 3 – 5 for silicon wafer. They are similar value with each other, meaning the negligible gap width changes among the different substrate at elevated temperatures. Linear thermal expansion coefficients of each metal and substrate material in a unit of $10^{-6}\mathrm{K}^{-1}$ are extracted from [57].

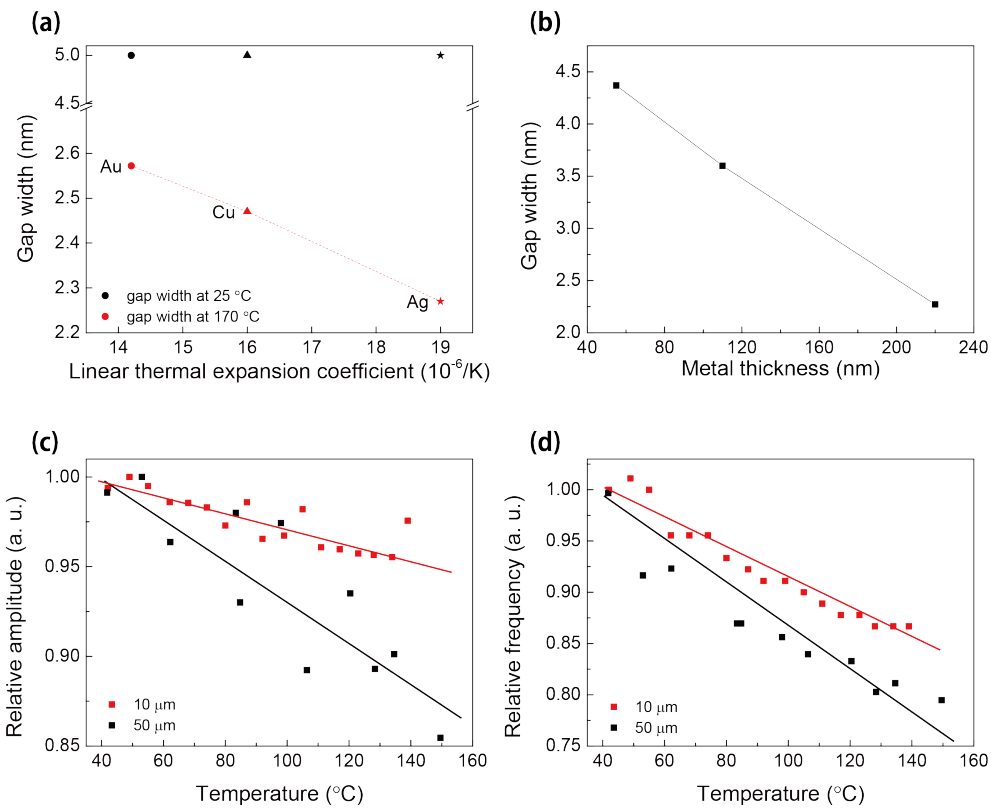

Figure 3.12: Various factors related to the thermal control of the gap width. Plots of (a) thermal expansion coefficients and (b) thickness of metals versus gap width from FEM calculation. (c) Measured relative amplitudes and (d) frequencies of air-filled rectangular ring-shaped nano-antennas with side length of 10 um $\times$ 40 um and 50 um $\times$ 50 um as a function of temperature.

Third, it can be expected from figure 3.10 (a) that if the nano-antennas become thinner, the effective gap width change is decreased. Finally, as the amount of thermal expansion of metals is proportional to the lateral size of the patterns, the effect of the pattern size of the nano-antennas on the THz resonant features should be important for the characterizaion of the therml control. I compared the THz resonant features of rectangular ring-shaped nano-antennas with different pattern sizes in figure 3.12 (c) and (d). In this experiment, the nano- antennas with the pattern size of 10 um and 50 um are compared. It is found that, during heating, the amount of changes in the gap width of the nano-antennas with 10 um wide pattern size is smaller than those with 50 um wide pattern size, confirming that the pattern size is of importance for the thermal control of the gap width of the nano-antennas.

3.7 Durability of air-filled nano-antennas according to the thermal control of air-filled nano-antennas

Permanent damage of metallic nano-antennas due to abrupt melting can be a significant disadvantage for various optical applications. For example, as shown in the schematic in figure 3.13 (a), debris along the nano-antennas formed during the lift-off process can be easily deformed during heating because the debris are in a shape of a thin sheet with a few nm thickness. I overcome the deformation problem by performing the ion milling of the surface of the nano-antennas with Ar ion beam at an oblique angle (80°). The graph in figure 3.13 (b) represents the effect of ion milling to prevent the permanent damage of the nano-antennas. The normalized amplitude of THz waves through unmilled nano-antennas decreases with temperature more steeply than that of milled ones. It is also found in unmilled nano-antenna samples #1 and #2 that the normalized amplitudes after cooling back are dependent on T_{max}. That is, during a cycle of heating and cooling back, the normalized amplitude of the nano-antennas with higher T_{max} is more reduced at room temperature, implying the steep decrease in the normalized amplitude stems from the permanent melting at T_{max}.

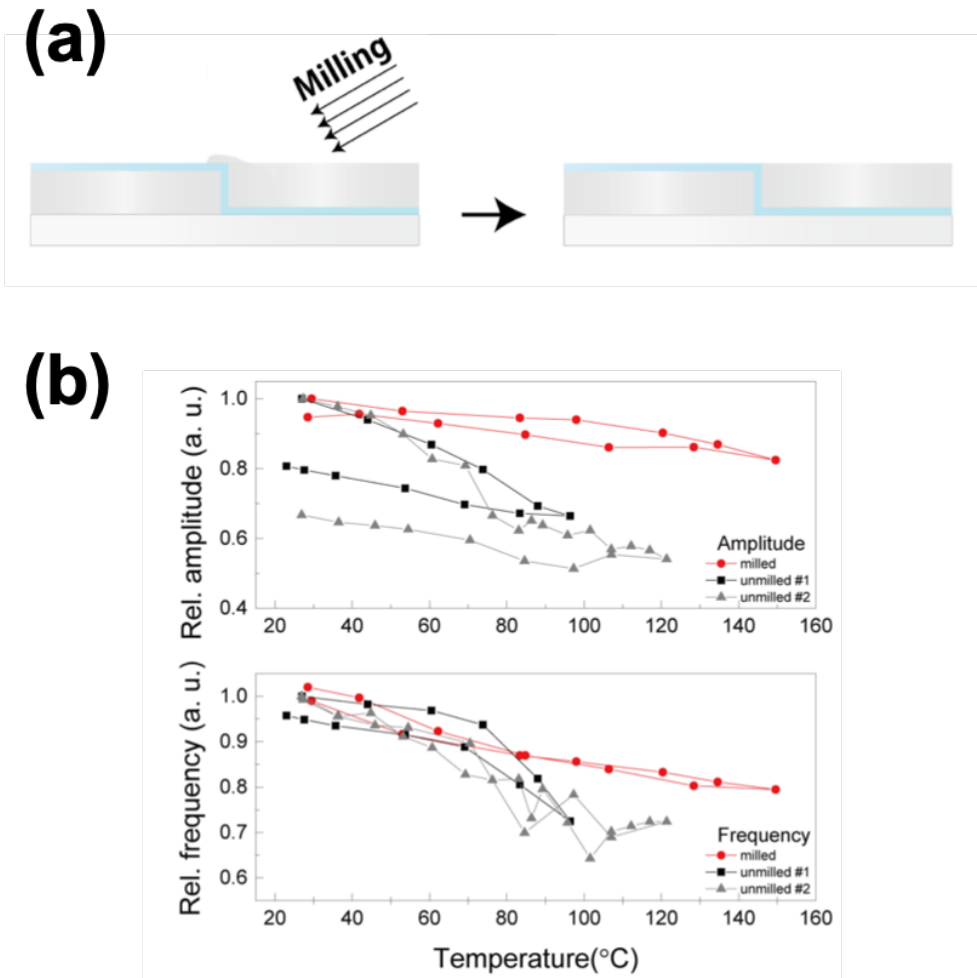

Figure 3.13: Effect of ion milling at slant angle on the performance of nano-antennas. (a) schematic of the ion milling process. (b) Relative amplitudes and frequencies of THz waves through nano-antennas with and without ion milling.

For the practical applications of the thermal control of THz waves, I show in figure 3.14 the resonant features of THz waves in a few cycles of heating and cooling. In spite of small amount of decrease in the normalized amplitude and the resonant frequency, the resonant features at 30 and 100 °C are still distinguishable.

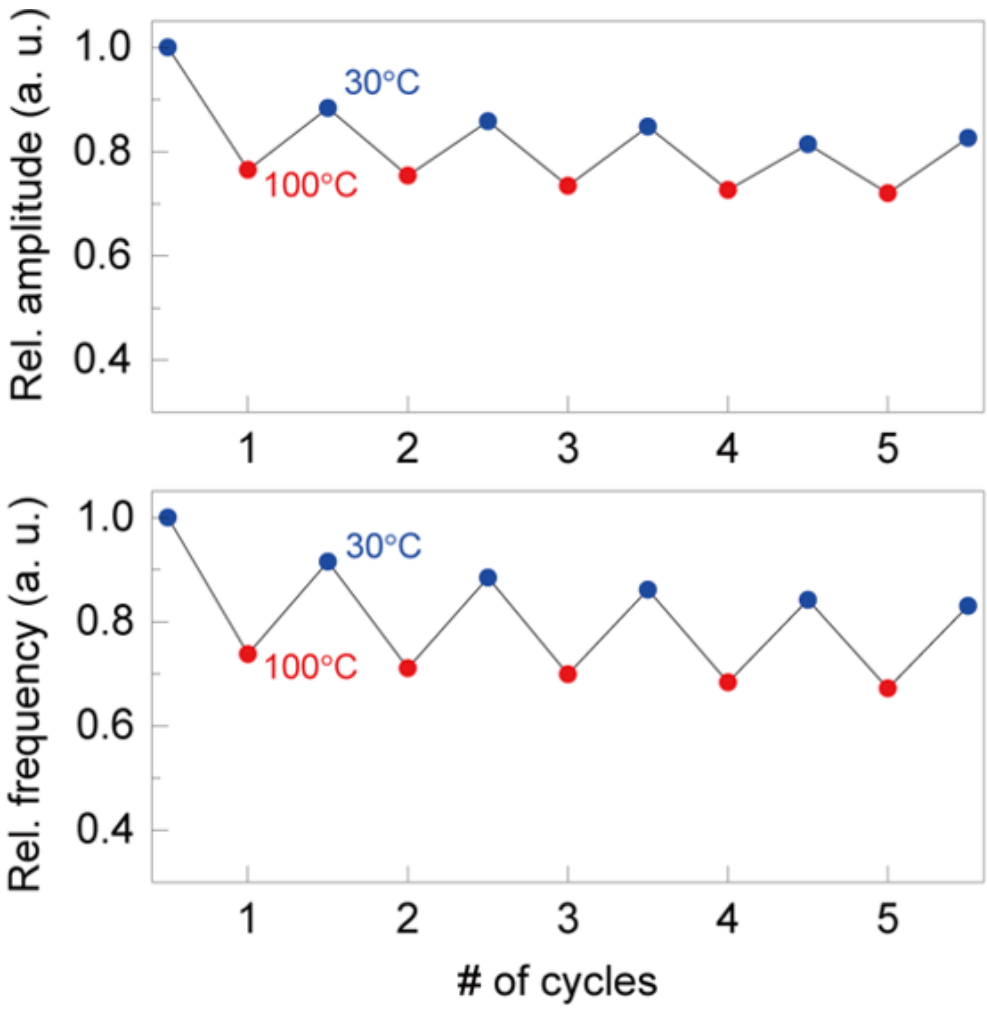

Figure 3.14: Normalized amplitudes (top) and resonant frequencies (bottom) of air-filled nano-antennas in several cycles of heating and cooling.

Chapter 4

Electrochemical amplification in 10 nm wide nano-electrodes

4.1 Introduction: Electrochemical cells and redox cycling

Electrochemistry is a branch of physical chemistry, which deals with the relation between electricity and chemical reactions. With electrodes and reactive species in contact, electrochemical reactions occur by an external potential applied on electrodes, or an electric current is generated by spontaneous chemical reactions. when electrochemical reaction takes place, electrons are transferred from an electrode to reactive species or vice versa. The electron transfer between electrodes and reactive species is called oxidation-reduction (redox) reaction simultaneously induced at each electrode. The device for electrochemical reaction is called an electrochemical cell, for example, such as an electrolytic cell shown in figure 4.1. One of the well-known electrochemical cells is metal- or ion-based electric batteries [58–63].

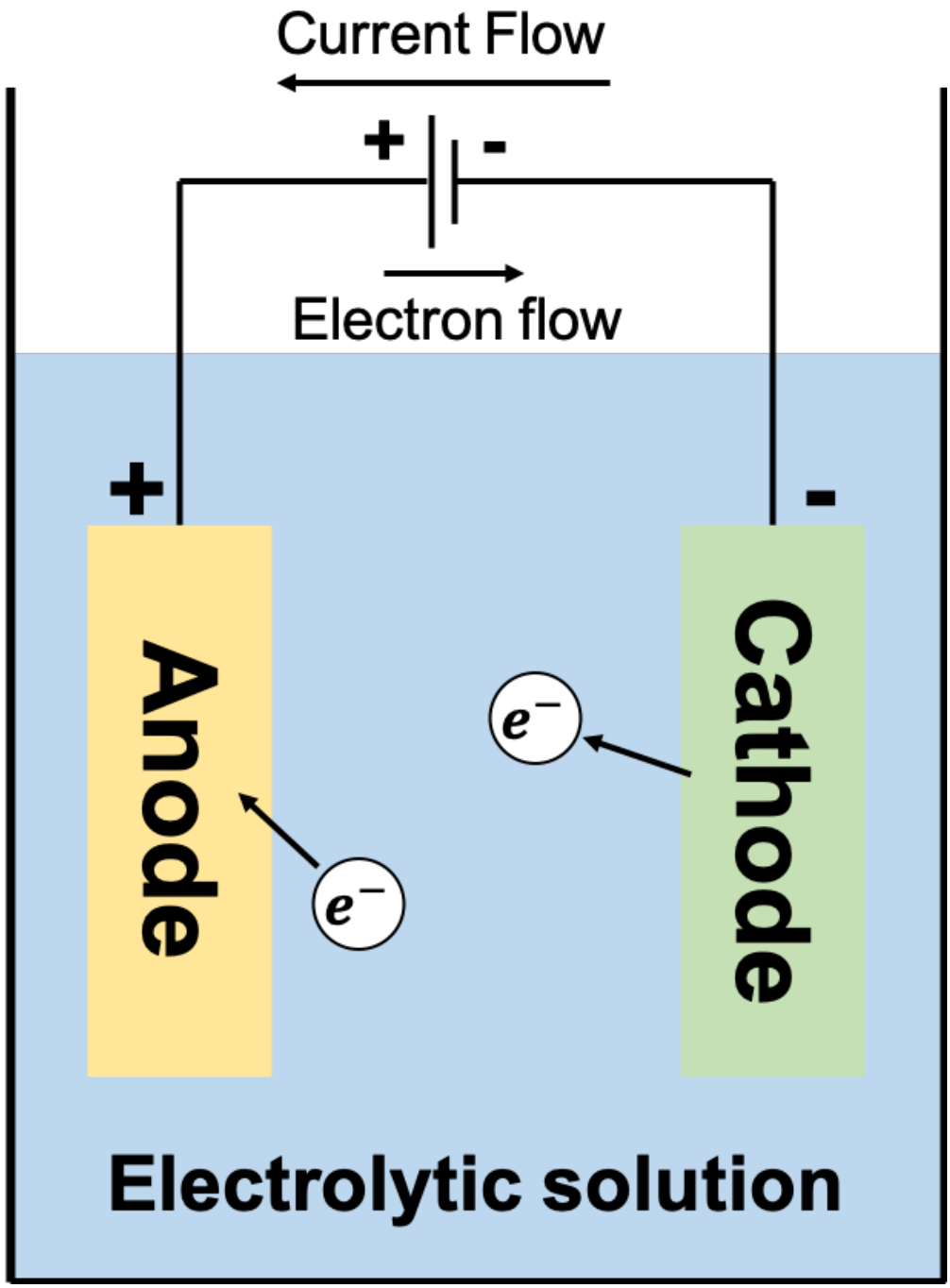

Figure 4.1: Schematic of an electrochemical cell. The electrochemical cell in this figure is called an electrolytic cell where a chemical reaction induced by external energy in forms of electric potential held at each electrode.

The reduction and oxidation reaction of the redox species at each electrode, namely anode and cathode have a negligible effect on one another if two electrodes are separated far away from each other. In other word, redox species is oxidized at the anode held at an oxidized potential and reduced at the cathode held at a reduced potential, and two reactions are not interfered by each other. If the separation between electrodes becomes narrower, however, the redox species, which is oxidized (reduced) at one electrode, can transported across the gap between electrodes by diffusion, migration or convection, and can be reduced (oxidized) at the other electrode. Thus one redox species trapped in the electrochemical cell with extremely small volume experiences successive redox reactions at a given measurement timescale. The successive redox reaction is called redox cycling. During the redox cycling, the Faradaic current from the redox cycling is highly amplified due to the successive reaction. In this chapter, I discuss the amplified Faradaic current from the redox cycling in the nano-electrodes fabricated by the modified atomic layer lithography similar with [27], achieving the narrowest gap distance of the electrochemical cell.

4.2 Calculation of Faradaic limiting current during redox cycling

For the detailed description of redox cycling, it is helpful to focus on electrochemical kinetics that governs redox cycling at the surface of electrodes. First of all, charge transfer between an electrode and specific redox species is related to the electric potential difference. According to the chemical kinetic theory, net current via charge transfer is a sum of the currents from the reduction and oxidation reaction, which is increased with the electric potential of the electrode and the equilibrium potential of the redox species. The relation is called Butler-Volmer equation:

$$j = j_0 \cdot \{\exp\{\frac{\alpha_a z F}{RT}(E - E_{eq})\} - \exp\{-\frac{\alpha_c z F}{RT}(E - E_{eq})\}\} \tag{4.1}$$

where j is electrode current density, j_o exchange current density, E eledtrode potential, E_{eq} equilibrium potential, T absolute temperature, z number of electrons involved in the electrode reaction, F Faraday constant, R universal gas constant, α_c cathodic charge transfer coefficient and α_a anodic charge transfer coefficient.

Butler-Volmer equation predicts that the Faradaic current is exponentially increased with the potential difference between an electrode and a redox species. However, the equation assumes that the concentration of the redox species at the electrode surface is constant. Indeed, the Faradaic current is saturated and decreased above a sufficiently high electrode potential when all the redox species at the electrode surface participate

in the electrochemical reaction (mass-transfer-limited condition). At this condition, the concentration of the redox species along two electrodes is in a steady state, and the main factor determining Faradaic current is the ion transport of the redox species from bulk to surface. The equation related to the flux of the redox species is called Nernst-Plank equation:

$$J = -D[\nabla c + \frac{zF}{RT} c(\nabla \phi)] \tag{4.2}$$

where J is diffusive flux density, D diffusivity (or, diffusion coefficient) of the chemical species, c the concentration of the species, z the valence of ionic species, R gas constant, T the temperature and ϕ the electric potential.

In the equation, ion flux (here, flux of redox species) is proportional to the gradient of the concentration of the redox species and the electric potential applied between two electrodes. For the sake of simplicity, if electrolyte is added into the electrochemical cell, the electrolyte is relocated to offset the electric field held on each electrode and forms the electric double layer as in figure 4.2. As a result, electric field across electrodes is only applied near the electrode surface, thus the second term of above equation, which describes the effect of electric field distribution on the ion flux, can be ignored. Therefore, the equation is simplified to $J = -D\nabla c$ and the gradient of ion concentration is the only parameter to be considered.

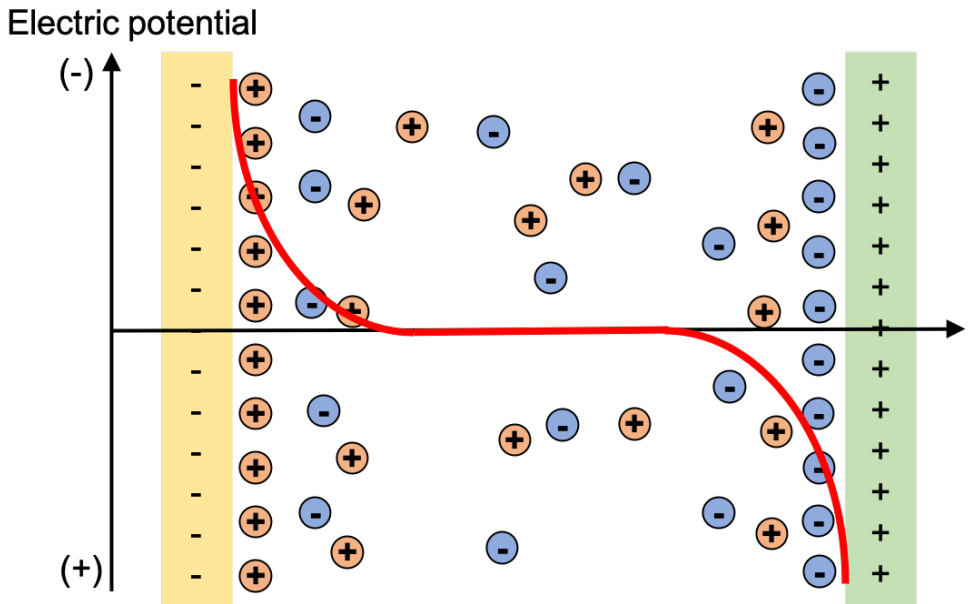

Figure 4.2: Schematic of an electric potential held between two electrodes filled with electrolytes. Cation and anion are relocated in order to offset an electric field across the electrochemical cell.

Now, with the assumption that the ion concentration along the gap separation is linear and the concentration of the reacted (reduced or oxidized) ion is zero at working electrode and c at reference electrode in a steady state of ion concentration, ion flux density can be calculated:

$$J = -D\frac{c}{d} \tag{4.3}$$

where d is the electrode distance. As the timescale of the charge transfer at the electrode surface is much smaller compared to that of ion diffusion, net Faradaic current measured at the electrode surface can be regarded as the ion flux across two electrodes [64]. That is, Faradaic current with sufficiently high electric potential of the working electrode is

$$i = \frac{neADC}{d} \tag{4.4}$$

where n is the number of electron transferred per molecule, e is the elementary charge, A is the area of each electrode. It is noteworthy in equation 4.4 that the Faradaic current is inversely proportional to the electrode distance d. At the same ion concentration, small electrode distance leads to the Faradaic current amplification of redox cycling, resulting in the improvement of the signal-to-noise ratio of the current for chemical reaction [65–68], biological detection [69, 70] and single-molecule detection [71, 72]. Moreover, decrease in the electrode distance also results in the amplified

Faradaic current during the electrolysis of pure water [73].

Meanwhile, with the development of nano-fabrications, the fabrication techniques of micro- and nano-electrodes for electrochemical cells have been extensively improved with suitable geometries for various applications [67, 74–82]. To the best of my knowledge, the narrowest electrode distance achieved in electrochemical cells for redox cycling is 37 nm from the literature survey [73]. However, the electrode distance of electrochemical cells can be narrower if other fabrication methods for nano-antennas, such as atomic layer lithography [23], are applied.

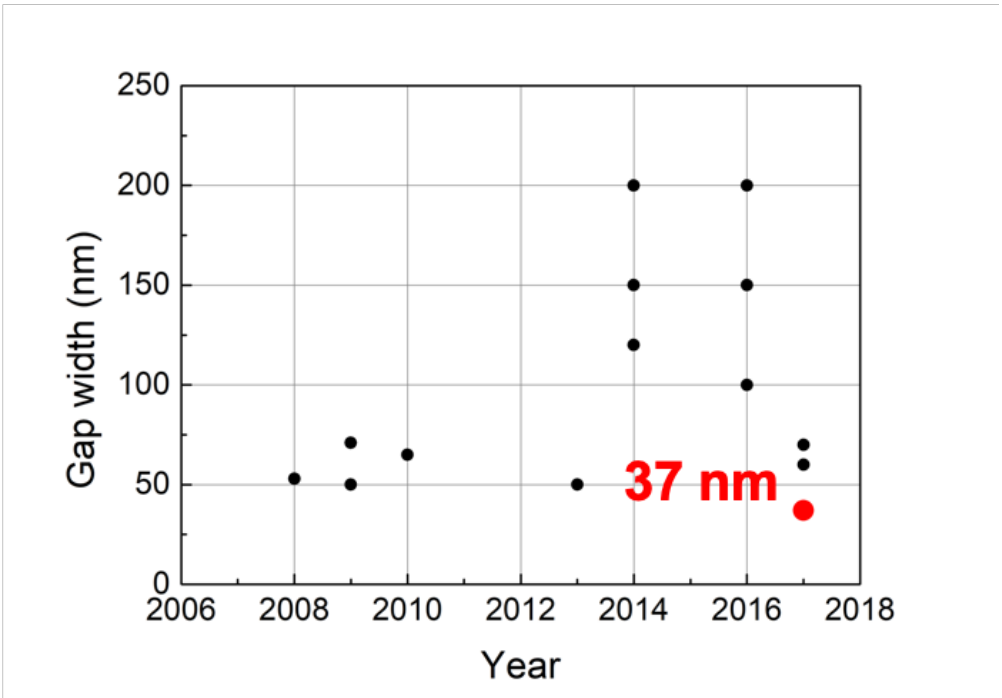

Figure 4.3: Electrode distance of various electrochemical cells from the literature. The narrowest electrode distance, to the best of our knowledge, is 37 nm.

4.3 Fabrication of 10 nm wide nano-electrodes using modified atomic layer lithography

Figure 4.4 shows the fabrication schematics of the nano-electrodes with modified atomic layer lithography [27]. First of all, slide glass substrates are cut into 4 pieces and pre-cleaned by ultrasonication in acetone and isopropyl alcohol (IPA) for 5 minutes, respectively, followed by drying with a nitrogen gas. Titanium (5 nm) and gold film (100 nm) is deposited on the substrates with an electron-beam evaporator with the pressure in the chamber at least 10^{-6} Torr and deposition rate kept at 0.5 Å/s.The acceleration voltage of the electron beam is 6.78 KeV and the emission current is in the range between 60 mA and 120 mA, depending on the deposition condition and the load of the crucible. On the Titanium/gold deposited substrates, AZ5214E image-reversal photoresist is patterned by using photolithography. Photoresist is spin-coated at the rate of 4000 rpm for 60 seconds, followed by soft baking on a hot plate at 90 °C for 90 seconds. After ultraviolet exposure for 6 seconds on a mask aligner with a photomask attached on the substrate, hard baking at 120 °C for 120 s and flood exposure of ultraviolet light for 40 seconds without a photomask, the substrate is dipped in MIF500 for 2 minutes for the development of the patterns and rinsed with distilled water. Vanadium (100 nm) is deposited on the patterned substrate with the same electron-beam evaporator and the photoresist is lifted off by ultrasonication in acetone. Here vanadium is selected as a sacrificial layer because it has about 5 times lower milling rate than

that of noble metal and it can be selectively etched in CR-7 [83]. After the deposition of vanadium, the gold film not covered with a vanadium film is removed by Ar ion milling, followed by ALD of 10 nm thick Al_2O_3. Titanium (5 nm) and gold (90 nm) is evaporated again and vanadium pattern, a sacrificial layer, is etched out by using CR-7, resulting in the successful fabrication of centimeter-long nanogap. dumbbell-like patterns consisting of nano-electrodes and contact pads for the current measurement are produced by photolithography, ion milling and lift-off of photoresist. Finally, by patterning photoresist again on top of metals on each side, to prevent the surface of metal from activation as an electrode, a pair of nano-electrodes for electrochemical experiments is completed after Al_2O_3 filled in the nano-electrode with 1M potassium hydroxide. Figure 4.5 (a) shows an optical image of nano-electrode and figure 4.5 (b)-(d) show top-view and cross-sectional SEM images of the electrodes. Nano-electrodes are well fabricated, and are 100 nm thick, 20 um long and 10 nm wide.

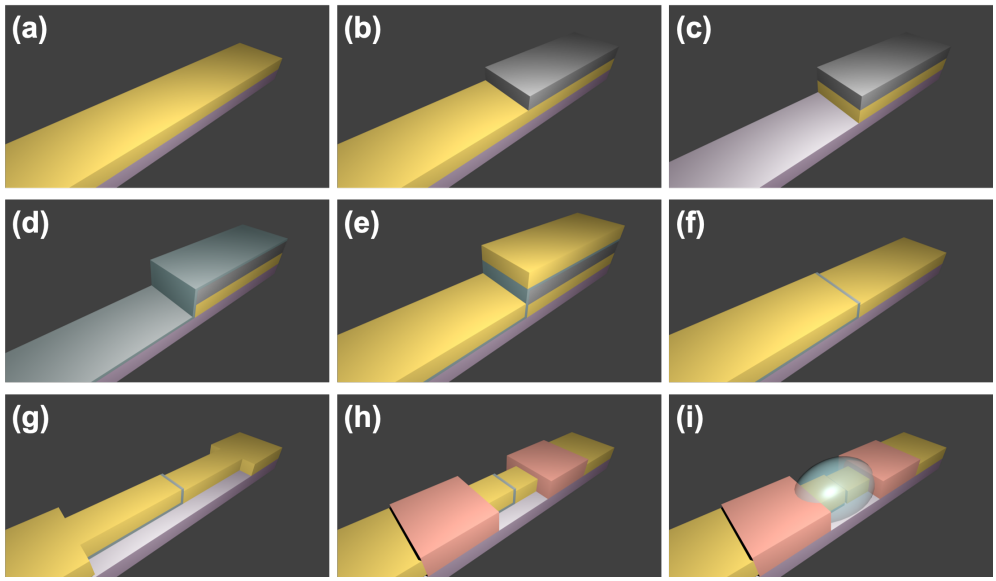

Figure 4.4: Fabrication schematics of side-by-side nano-electrodes. (a) Titanium/gold film deposition. (b) Vanadium patterning on Ti/Au film by photolithography and e-beam evaporation. (c) Ion milling for Au pattering (d) Atomic layer deposition of Al_2O_3 for a gap material. (e) Titanium/gold deposition to form nano-electrodes. (f) Removal of vanadium by wet etching to reveal nanogaps. (g) Electrode pattering for the fabrication of contact pads. (h) Photoresist pattering for the passivation of the upper part of the electrodes. (i) Chemical etching of Al_2O_3 for access into the nano-electrodes.

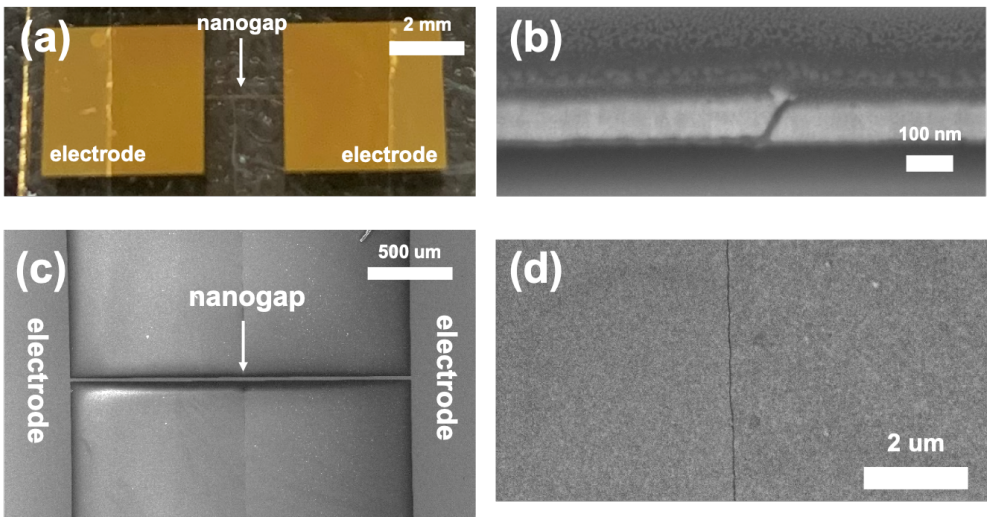

Figure 4.5: Optical and SEM images of a nano-electrode. (a) An optical image of a nano-electrode. nanogap is at the center of the bridge connecting the contact pads. (b) A cross-sectional SEM image of the nano-electrode. the electrode is 100 nm thick, 20 um long and 10 nm wide. (c) and (d) top-view images of the nano-electrode.

4.4 Fabrication issue: Electrostatic damage (ESD) of nano-electrodes

During the fabrication of 10 nm wide nano-electrodes, damage in the nanogap such as SEM images in figure 4.6 is observed in some of the nano-electrode patterns, which highly decreases the fabrication yield of the nano-antennas. The origin of the fabrication issue may result from the electrostatic damage (ESD) at the electrode which were electrically insulated before ESD. In details, as the scale of nanostructures decreases to a few nanometers, the nanostructures lie on a quantum regime where electron tunneling is possible at a moderate potential applied, resulting in optical nonlinearity or dielectric breakdown under DC voltage. Meanwhile, the electric potential held on a human body due to the electrostatic accumulation is about 10 kV, and it is extremely high compared to the voltage to induce dielectric breakdown [84]. If each side of the nano-electrode is electrically isolated from each other, the electrostatic potential from a human body is enough to break the nano-electrode. In the SEM image shown in figure 4.6, the width of the nano-electrode increases to several micrometers during the fabrication or after electrochemical measurements are conducted. Interestingly, the gap of the nano-electrode is symmetrically broadened to each electrode, demonstrating that the damage on the electrode is not originated from the fabrication error such as unintended lift-off of one side of the electrode. ESD is an inevitable phenomenon in electrochemical cells with electrode distance at nanoscale, thus should be prevented

for the improvement in electrochemical cells.

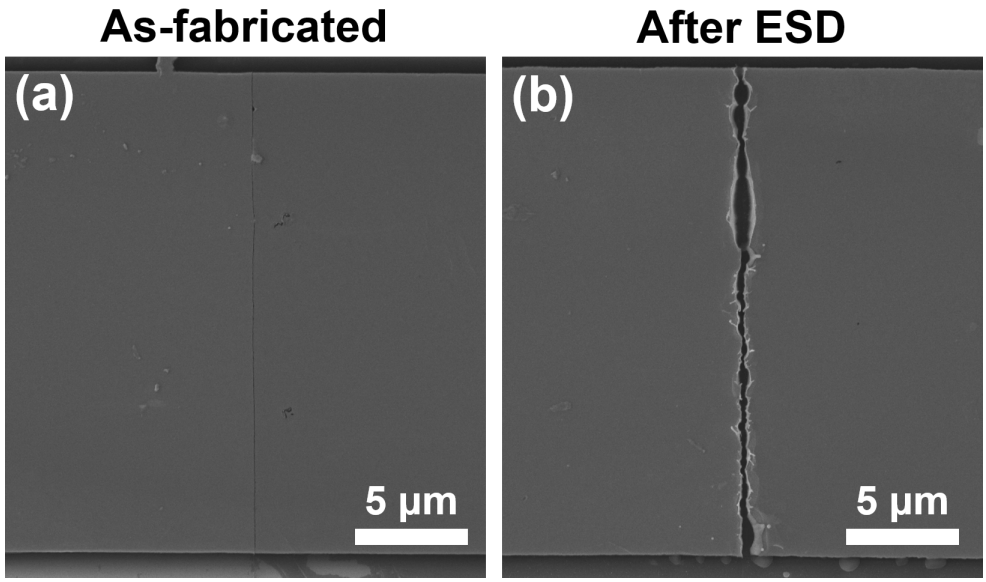

Figure 4.6: SEM images of a nano-electrode before (a) and after (b) electrostatic damage. Once damaged, the gap width of the nano-electrode is broadened from 10 nm to several microns.

To prevent ESD, it is required to wear the gloves, wrist straps and a conductive coat that are grounded. However, some samples are readily damaged before the measurement, which might happen during fabricating or handling the samples. The ESD problems during the fabrication can be overcome by fabricating the nano-electrode pattern that all sides of the electrodes on a substrate is electrically connected and grounded as in figure 4.7. By doing this, considering that electrostatic charge is still accumulated in the electrodes, the charge accumulation does not damage the nano-electrode anymore. Each pattern can be used for the electrochemical measurement after attaching a fabric conductive tape connected to a potentiostat and cutting the edge of the metal surface.

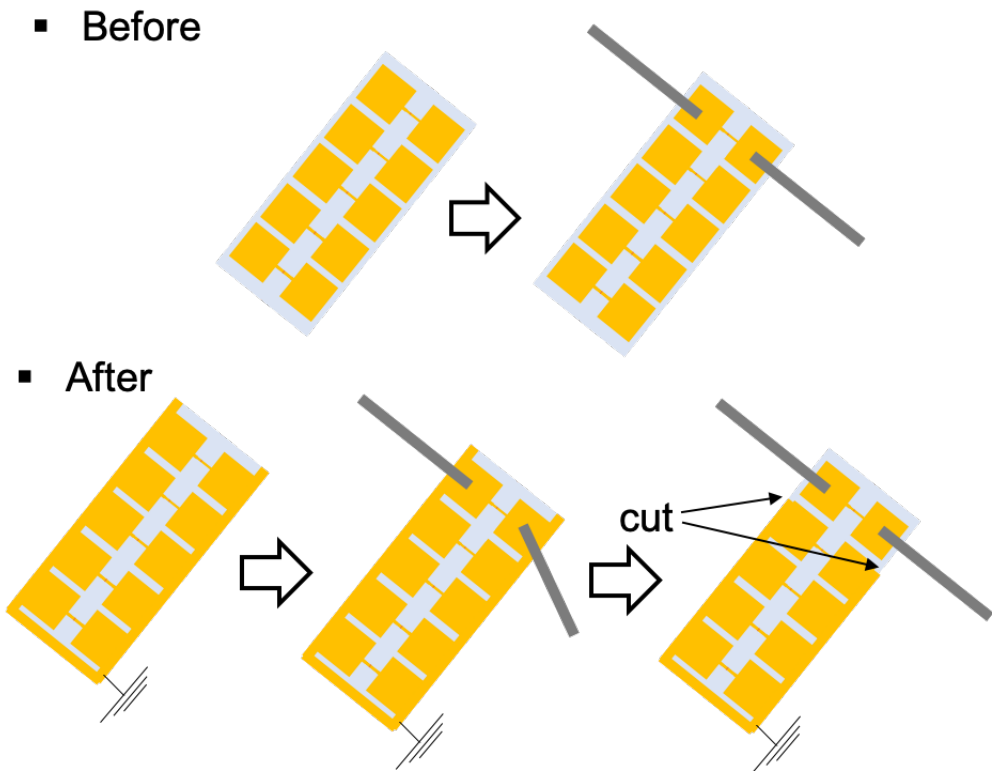

Figure 4.7: Schematic of the nano-electrode pattern to prevent ESD.

4.5 Measurement of Faradaic current with 10 nm wide nano-electrodes

For the electrochemical experiment, a potentiostat with three-electrode system (CH Instrument) is used. A Ag/AgCl reference electrode is positioned in a droplet solution filled on and in nano-electrodes. During carrying out the experiment, the left electrode (the generator electrode) is swept from -0.2 V to 0.4 V vs Ag/AgCl while the right electrode (the collector electrode) is kept in a constant oxidizing potential of 0.2 V vs Ag/AgCl as shown in figure 4.8.

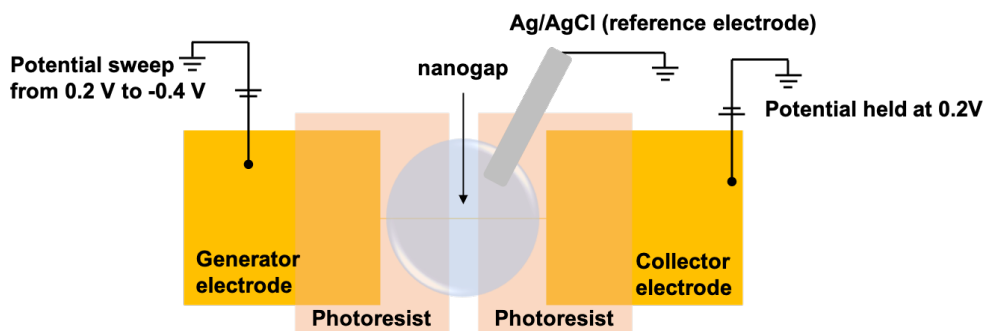

Figure 4.8: Schematic of experimental setup for cyclic voltammetry.

Nano-electrode for the electrochemical experiment is carefully prepared to prevent ESD and is kept in wet condition during the experiment as shown in figure 4.9. First, a fabric conductive tape is attached on each electrode with electric circuit closed, grounded and connected to a potentiostat. After all the electric connections are completed, one pair of the nano-electrode is isolated from the others. Next, Al_2O_3 filled in the nano-electrode is etched out with 1 M KOH, and the solution is replaced with

deionized water and the target solution, which is 0.5 mM $[(Ru(NH_3)_6]Cl_2$ in a 1 M KNO_3 aqueous solution (Sigma Aldrich), successively.

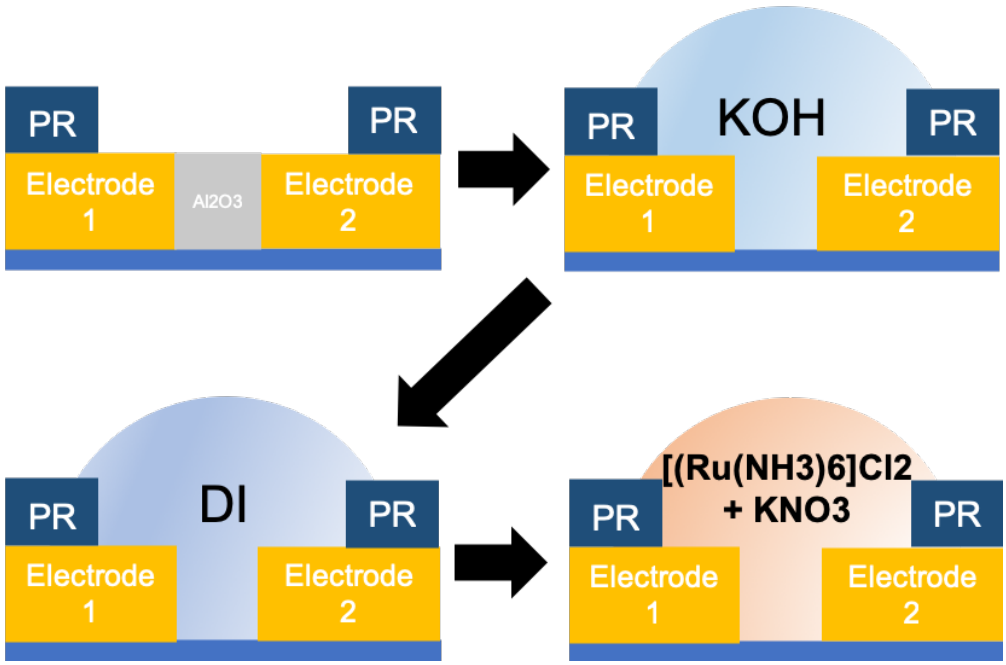

Figure 4.9: Schematics of preparation of nano-electrodes with redox species filled.

Figure 4.10 presents cyclic voltammograms for the nano-electrode filled in different solutions. First, I conduct cyclic voltammetry with KNO_3 solution without $[(Ru(NH_3)_6]Cl_2$ filled in to measure background currents. Then, the solution is replaced with $[(Ru(NH_3)_6]Cl_2$ and KNO_3 solution. the limiting current of 13.368 nA at -0.4 V is measured at the right (collector) electrode with the background current subtracted. As the measured current is a sum of the currents from upper and side part of the electrode, the current from upper part should be excluded to obtain the current only from the side part of the nano-electrode. Thus, the solution is dried after diluted in water and placed again on

the electrode to keep the side part of the electrode in touch with air. The current from the side part of the electrode is shown to be 7.43 nA as shown in the right schematic in figure 4.10. Therefore, the current from the upper and side part are shown to be 5.938 nA and 7.43 nA, respectively.

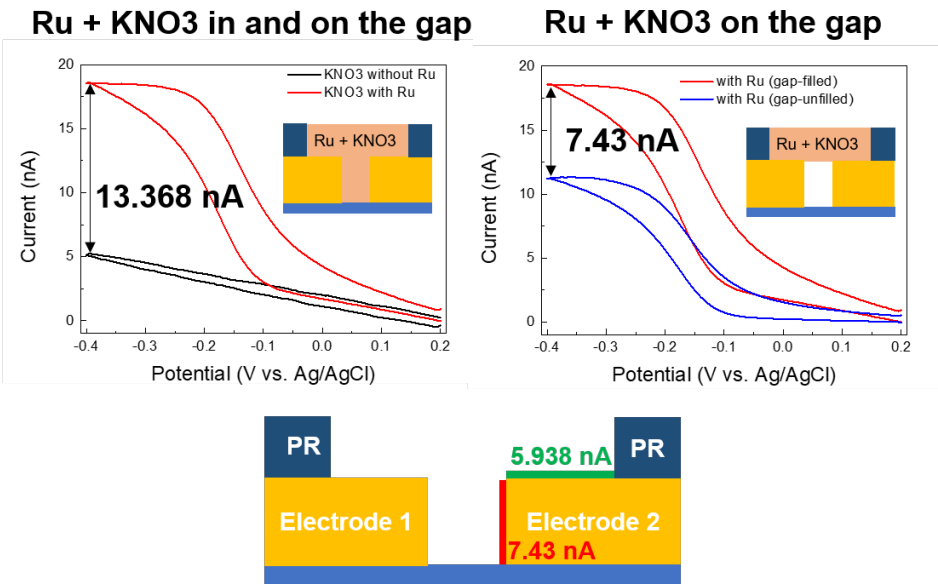

Figure 4.10: Cyclic voltammogram of redox cycling.

I compare the current measured from the collector electrode, i_{exp}, with the theoretical Faradaic limiting current for two opposite electrodes, $i_{cal} = neADC/d$, with n = 1, e = 1.6×10^{-19} C, A = 103 nm $\times$ 20 um = 2.07×10^{6} mm^2, D = 0.63×10^{6} nm^2/s, C = $0.5 \times 6.02 \times 10^{-4}$ nm^{-3} and d = 10 nm. The calculation shows that i_{cal} = 6.28 nA, which is in good agreement with i_{exp} = 7.43 nA. Discrepancy between two values may stem from the geometry of electrodes open to the bulk solution on top of the electrodes so that reacted redox species on upper part of one electrode can be transported to the

other electrode by diffusion. Figure 4.11 presents the current from the experiment and the calculation as a function of the gap width, d, implying that the Faradaic current will be more amplified if the gap width becomes narrower.

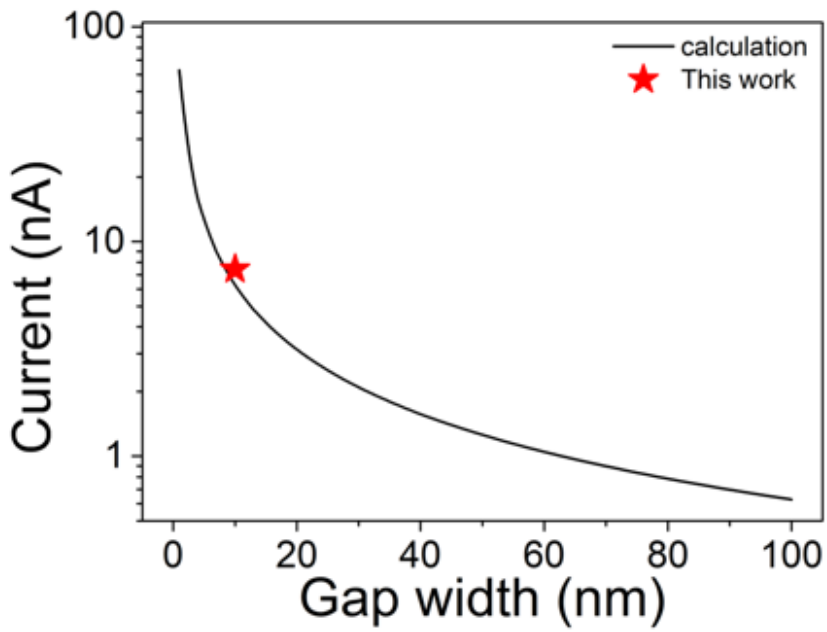

Figure 4.11: Calculated (line) and experimental (star) Faradaic limiting current.

To show the advantage of the fabrication method of nano-electrode used in this chapter, Faradaic limiting current from the numerical calculation [85] and the experimental data [68] are compared. these studies dealing with redox cycling in side-by-side nano-electrodes are selected because it is hard to determine an effective area of electrodes related to the redox cycling in many electrochemical cells with laminate structures [67, 73, 86]. Figure 4.12 shows the Faradaic current normalized by an electrode area and bulk ion concentration of redox species as a function of the electrode distance.

i_{exp} from 10 nm wide nano-electrode in our experiment is about 7 times higher than the current from 70 nm wide nano-electrode from [68], demonstrating Faradaic limiting current is inversely proportional to the electrode distance. Fitting current-distance data points with inversely proportional function, $i \propto 1/d$ relation demonstrated in numerical simulation [85] is extended to 10 nm distance with good agreement. Moreover, with further decrease in the electrode distance, Faradaic current can be much more amplified unless additional effects arise as a result of quantum phenomena, that would be ignored at a large electrode distance.

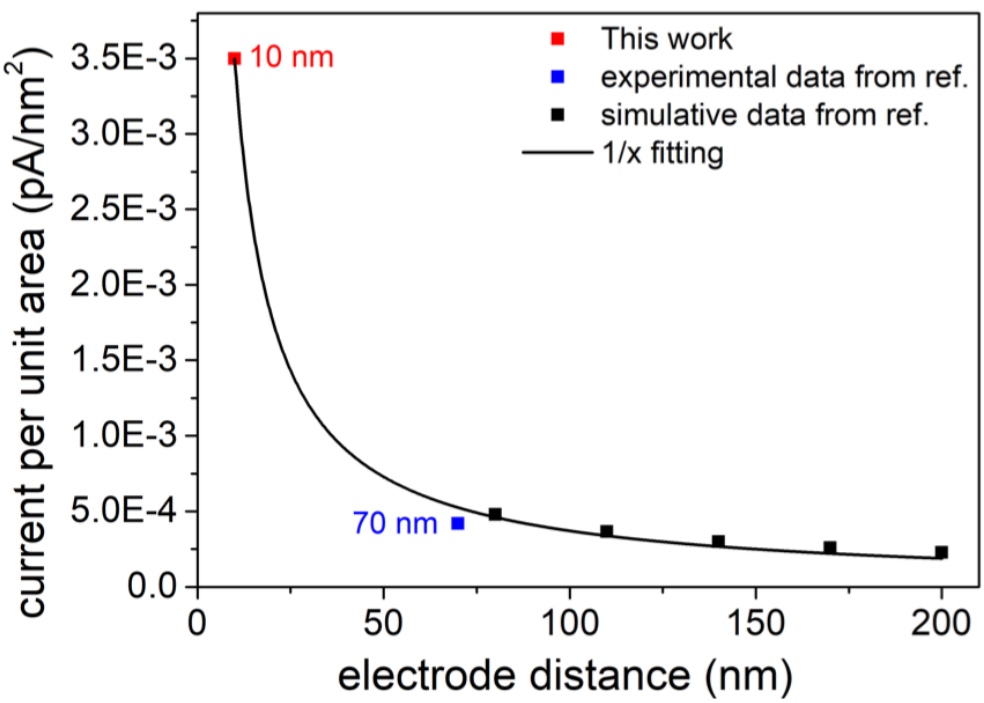

Figure 4.12: Plots of Faradaic limiting currents among [85], [68] and this work. Electrode area and ion concentration in these works are normalized to correct the same experimental condition.

Chapter 5

Conclusion

In this thesis, I performed air-filled nanogap fabrication for various optical and electrochemical applications by chemically etching dielectric spacer filled in nanogaps fabricated by atomic layer lithography technique. The full-etching of the dielectric spacer is confirmed by measuring THz transmission spectra and the EDS maps from TEM before and after the etching process. For the application of the air-filled nanogaps as nano-antennas, active thermal control of THz waves through the nano-antennas is achieved. The origin of the thermal control is proven to be thermal expansion of metals, resulting in the reduction of the gap width. I also compared various factors affecting THz resonant features such as pattern size, gap width, metal thickness and the dielectric spacer. the results are theoretically supported by the FEM calculation and the coupled-mode calculation.

Meanwhile, water-filled nanogaps can be fabricated during the etching process and be utilized for the electrochemical amplifications. As redox reactions at electrodes

are amplified with decreasing the electrode distance, the nano-electrodes with narrow electrode distance have an advantage in the electrochemical applications. I fabricated 10 nm wide nano-electrode filled with redox species, by using modified atomic layer lithography technique, and achieved the narrowest nano-electrode to the best of our knowledge. I also observed the amplified Faradaic limiting current during redox cycling and compared the resulting current per unit area with those measured in previous studies.

Chapter 6

Appendix

6.1 Terahertz time-domain spectroscopy

Schematics of THz-TDS setup is illustrated in figure 6.1. In the experimental setup used in this thesis, a laser with wavelength of 532 nm and power of 4 W pumps a Ti:sapphire cavity in order to generate 130 fs pulse train with center wavelength of 800 nm and 80 MHz repetition rate. The pulse train is divided into two parts. one part is a pump beam, which excite a DC-biased low-temperature grown gallium arsenide (LT-GaAs) emitter to generate THz pulses with peak frequency at 0.5 THz. Generated THz pulse is collected and focused on a sample by parabolic mirror, and THz pulse transmitting sample is collected and focused on a zinc telluride (ZnTe) crystal. The other part of the pulse train is a probe beam which is also focused on a ZnTe crystal of which optical response is changed by an intensity of THz pulse because of its nonlinear behavior. Birefringent property of ZnTe slightly changes the polarization of

probe beam which is later divided into two beams with different polarization direction while going through wollaston prism, measured by balanced photodetector. From relative intensity difference between two probe beams at the photodetector, intensity of THz pulse at specific time delay between THz pulse and probe beam is calculated. The detection technique is called electro-optic sampling (EO sampling). measured THz intensity in time scale is converted to frequency domain spectrum by Fourier transform, and the THz spectrum through the sample on 2 mm $\times$ 2 mm aluminum aperture is normalized by that through the aperture to obtain normalized amplitude.

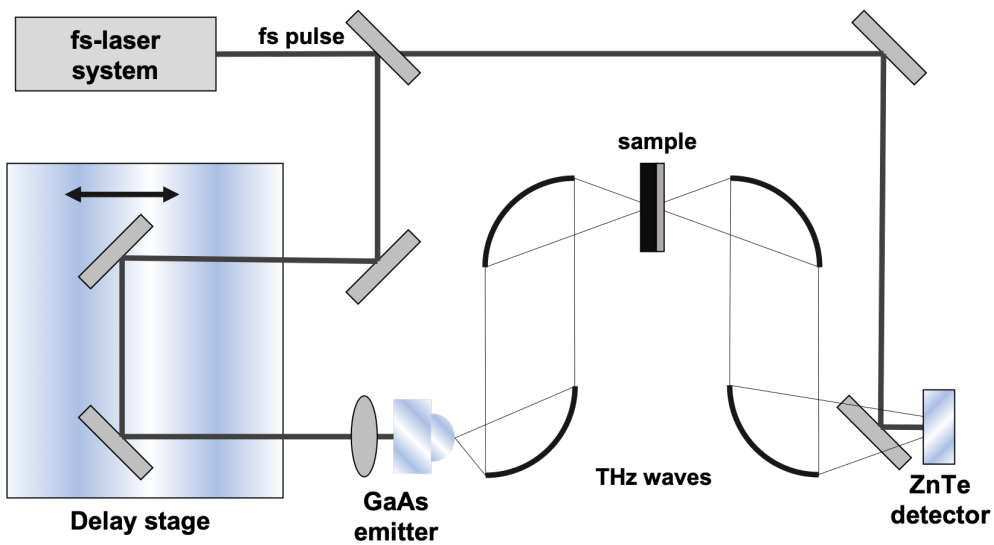

Figure 6.1: Schematic of a THz time-domain spectroscopy setup.

Bibliography

[1]T. W. Ebbesen, H. J. Lezec, H. F. Ghaemi, T. Thio, and P. A. Wolff, "Extraordinary optical transmission through sub-wavelength hole arrays", Nature **391**, 667–669 (1998).

[2]M. Fleischmann, P. Hendra, and A. McQuillan, "Raman spectra of pyridine adsorbed at a silver electrode", Chemical Physics Letters **26**, 163–166 (1974).

[3]K. Kneipp, Y. Wang, H. Kneipp, L. T. Perelman, I. Itzkan, R. R. Dasari, and M. S. Feld, "Single molecule detection using surface-enhanced raman scattering (SERS)", Phys. Rev. Lett. **78**, 1667–1670 (1997).

[4]H. Xu, E. J. Bjerneld, M. Käll, and L. Börjesson, "Spectroscopy of single hemoglobin molecules by surface enhanced raman scattering", Phys. Rev. Lett. **83**, 4357–4360 (1999).

[5]Y. C. Cao, R. Jin, and C. A. Mirkin, "Nanoparticles with raman spectroscopic fingerprints for DNA and RNA detection", Science **297**, 1536 (2002).

[6]S.-H. Lim, A. G. Caster, and S. R. Leone, "Single-pulse phase-control interferometric coherent anti-stokes raman scattering spectroscopy", Phys. Rev. A **72**, 041803 (2005).

[7]E. N. Esenturk and A. R. H. Walker, "Surface-enhanced raman scattering spectroscopy via gold nanostars", Journal of Raman Spectroscopy **40**, 86–91 (2009).

[8]W. Kim, N. Kim, E. Lee, D. Kim, Z. Hwan Kim, and J. Won Park, "A tunable au core–ag shell nanoparticle tip for tip-enhanced spectroscopy", The Analyst **141**, 5066–5070 (2016).

[9]K. Shin and H. Chung, "A au nanoparticle-incorporated sponge as a versatile transmission surface-enhanced raman scattering substrate", The Analyst **140**, 5074–5081 (2015).

[10]M. A. Seo, H. R. Park, S. M. Koo, D. J. Park, J. H. Kang, O. K. Suwal, S. S. Choi, P. C. M. Planken, G. S. Park, N. K. Park, Q. H. Park, and D. S. Kim, "Terahertz field enhancement by a metallic nano slit operating beyond the skin-depth limit", Nature Photonics **3**, 152–156 (2009).

[11]H. A. Atwater and A. Polman, "Plasmonics for improved photovoltaic devices", Nature Materials **9**, 205–213 (2010).

[12]L. Ju, B. Geng, J. Horng, C. Girit, M. Martin, Z. Hao, H. A. Bechtel, X. Liang, A. Zettl, Y. R. Shen, and F. Wang, "Graphene plasmonics for tunable terahertz metamaterials", Nature Nanotechnology **6**, 630–634 (2011).

[13]D.-K. Lim, K.-S. Jeon, J.-H. Hwang, H. Kim, S. Kwon, Y. D. Suh, and J.-M. Nam, "Highly uniform and reproducible surface-enhanced raman scattering from DNA-tailorable nanoparticles with 1-nm interior gap", Nature Nanotechnology **6**, 452–460 (2011).

[14]H. Im, K. C. Bantz, S. H. Lee, T. W. Johnson, C. L. Haynes, and S.-H. Oh, "Self-assembled plasmonic nanoring cavity arrays for SERS and LSPR biosensing", Advanced Materials **25**, 2678–2685 (2013).

[15]M. A. Kaliteevski, S. Brand, J. Garvie-Cook, R. A. Abram, and J. M. Chamberlain, "Terahertz filter based on refractive properties of metallic photonic crystal", Optics Express **16**, 7330 (2008).

[16]C. R. Williams, S. R. Andrews, S. A. Maier, A. I. Fernández-Domínguez, L. Martín-Moreno, and F. J. García-Vidal, "Highly confined guiding of terahertz surface plasmon polaritons on structured metal surfaces", Nature Photonics **2**, 175–179 (2008).

[17]P. Upadhyaya, S. Pramanik, and S. Bandyopadhyay, "Optical transitions in a quantum wire with spin-orbit interaction and its applications in terahertz electronics: beyond zeroth-order theory", Physical Review B **77**, 155439 (2008).

[18]M. C. Hoffmann, B. S. Monozon, D. Livshits, E. U. Rafailov, and D. Turchinovich, "Terahertz electro-absorption effect enabling femtosecond all-optical switching in semiconductor quantum dots", Applied Physics Letters **97**, 231108 (2010).

[19]S.-P. Han, N. Kim, W.-H. Lee, E. S. Lee, H. Ko, I.-M. Lee, K. Moon, D. H. Lee, and K. H. Park, "Real-time imaging of moving living objects using a compact terahertz scanner", Applied Physics Express **9**, 022501 (2016).

[20]J. Lee, M. Seo, D. Park, D. Kim, S. Jeoung, C. Lienau, Q.-H. Park, and P. Planken, "Shape resonance omni-directional terahertz filters with near-unity transmittance", Optics Express **14**, 1253 (2006).

[21]D. J. Park, S. B. Choi, Y. H. Ahn, F. Rotermund, I. B. Sohn, C. Kang, M. S. Jeong, and D. S. Kim, "Terahertz near-field enhancement in narrow rectangular apertures on metal film", Optics Express **17**, 12493 (2009).

[22]H.-R. Park, K. J. Ahn, S. Han, Y.-M. Bahk, N. Park, and D.-S. Kim, "Colossal absorption of molecules inside single terahertz nanoantennas", Nano Letters **13**, 1782–1786 (2013).

[23]X. Chen, H.-R. Park, M. Pelton, X. Piao, N. C. Lindquist, H. Im, Y. J. Kim, J. S. Ahn, K. J. Ahn, N. Park, D.-S. Kim, and S.-H. Oh, "Atomic layer lithography of wafer-scale nanogap arrays for extreme confinement of electromagnetic waves", Nature Communications **4**, 2361 (2013).

[24]J. S. Ahn, T. Kang, D. K. Singh, Y.-M. Bahk, H. Lee, S. B. Choi, and D.-S. Kim, "Optical field enhancement of nanometer-sized gaps at near-infrared frequencies", Optics Express **23**, 4897 (2015).

[25]T. Kang, J. Rhie, J. Park, Y.-M. Bahk, J. S. Ahn, H. Jeon, and D.-S. Kim, "Resonance tuning of electric field enhancement of nanogaps", Applied Physics Express **8**, 092003 (2015).

[26]H. Yang, D.-S. Kim, R. H.J.-Y. Kim, J. S. Ahn, T. Kang, J. Jeong, and D. Lee, "Magnetic nature of light transmission through a 5-nm gap", Scientific Reports **8**, 2751 (2018).

[27]J. Jeong, J. Rhie, W. Jeon, C. S. Hwang, and D.-S. Kim, "High-throughput fabrication of infinitely long 10 nm slit arrays for terahertz applications", Journal of Infrared, Millimeter, and Terahertz Waves **36**, 262–268 (2015).

[28]J.-Y. Kim, B. J. Kang, J. Park, Y.-M. Bahk, W. T. Kim, J. Rhie, H. Jeon, F. Rotermund, and D.-S. Kim, "Terahertz quantum plasmonics of nanoslot antennas in nonlinear regime", Nano Letters **15**, 6683–6688 (2015).

[29]S. Han, Y.-M. Bahk, N. Park, and D.-S. Kim, "Terahertz field enhancement in asymmetric and tapered nano-gaps", Optics Express **24**, 2065–2071 (2016).

[30]S. Han, J.-Y. Kim, T. Kang, Y.-M. Bahk, J. Rhie, B. J. Kang, Y. S. Kim, J. Park, W. T. Kim, H. Jeon, F. Rotermund, and D.-S. Kim, "Colossal terahertz nonlinearity in angstrom- and nanometer-sized gaps", ACS Photonics **3**, 1440–1445 (2016).

[31]Y.-M. Bahk, S. Han, J. Rhie, J. Park, H. Jeon, N. Park, and D.-S. Kim, "Ultimate terahertz field enhancement of single nanoslits", Physical Review B **95**, 075424 (2017).

[32]O. K. Suwal, J. Rhie, N. Kim, and D.-S. Kim, "Nonresonant 104 terahertz field enhancement with 5-nm slits", Scientific Reports **7**, 45638 (2017).

[33]N. Kim, S. In, D. Lee, J. Rhie, J. Jeong, D.-S. Kim, and N. Park, "Colossal terahertz field enhancement using split-ring resonators with a sub-10 nm gap", ACS Photonics **5**, 278–283 (2018).

[34]D. Kim, J. Jeong, G. Choi, Y.-M. Bahk, T. Kang, D. Lee, B. Thusa, and D.-S. Kim, "Giant field enhancements in ultrathin nanoslots above 1 terahertz", ACS Photonics **5**, 1885–1890 (2018).

[35]J. Rhie, D. Lee, Y.-M. Bahk, J. Jeong, G. Choi, Y. Lee, S. Kim, S. Hong, and D.-S. Kim, "Control of optical nanometer gap shapes made via standard lithography using atomic layer deposition", Journal of Micro/Nanolithography, MEMS, and MOEMS **17**, 1 (2018).

[36]T. Kang, R. H.J.-Y. Kim, G. Choi, J. Lee, H. Park, H. Jeon, C.-H. Park, and D.-S. Kim, "Terahertz rectification in ring-shaped quantum barriers", Nature Communications **9**, 4914 (2018).

[37]K. Lee, J. Jeong, Y.-M. Bahk, J. Rhie, I.-K. Baek, B. J. Lee, Y. H. Kang, S. Hong, G.-S. Park, and D.-S. Kim, "Microwave funneling through sub-10 nm nanogaps", ACS Photonics **3**, 537–542 (2016).

[38]Y.-G. Jeong, S. Han, J. Rhie, J.-S. Kyoung, J.-W. Choi, N. Park, S. Hong, B.-J. Kim, H.-T. Kim, and D.-S. Kim, "A vanadium dioxide metamaterial disengaged from insulator-toMetal transition", Nano Letters **15**, 6318–6323 (2015).

[39]W. Park, J. Rhie, N. Y. Kim, S. Hong, and D.-S. Kim, "Sub-10 nm feature chromium photomasks for contact lithography patterning of square metal ring arrays", Scientific Reports **6**, 23823 (2016).

[40]G. Choi, Y.-M. Bahk, T. Kang, Y. Lee, B. H. Son, Y. H. Ahn, M. Seo, and D.-S. Kim, "Terahertz nanoprobing of semiconductor surface dynamics", Nano Letters **17**, 6397–6401 (2017).

[41]H.-R. Park, X. Chen, N.-C. Nguyen, J. Peraire, and S.-H. Oh, "Nanogap-enhanced terahertz sensing of 1 nm thick (lambda/10(6)) dielectric films", Acs Photonics **2**, 417–424 (2015).

[42]Z. Ma, C. Jiang, W. Yuan, and Y. He, "Large-scale patterning of hydrophobic silicon nanostructure arrays fabricated by dual lithography and deep reactive ion etching", Nano-Micro Letters **5**, 7–12 (2013).

[43]F. J. Garcia-Vidal, L. Martin-Moreno, T. W. Ebbesen, and L. Kuipers, "Light passing through subwavelength apertures", Reviews of Modern Physics **82**, 729–787 (2010).

[44]Y.-M. Bahk, B. J. Kang, Y. S. Kim, J.-Y. Kim, W. T. Kim, T. Y. Kim, T. Kang, J. Rhie, S. Han, C.-H. Park, F. Rotermund, and D.-S. Kim, "Electromagnetic saturation of

angstrom-sized quantum barriers at terahertz frequencies", Physical Review Letters **115**, 125501 (2015).

[45]J. F. Li, Y. F. Huang, Y. Ding, Z. L. Yang, S. B. Li, X. S. Zhou, F. R. Fan, W. Zhang, Z. Y. Zhou, D. Y. Wu, B. Ren, Z. L. Wang, and Z. Q. Tian, "Shell-isolated nanoparticle-enhanced raman spectroscopy", Nature **464**, 392–395 (2010).

[46]H. Aouani, M. Rahmani, M. Navarro-Cia, and S. A. Maier, "Third-harmonic-upconversion enhancement from a single semiconductor nanoparticle coupled to a plasmonic antenna", Nature Nanotechnology **9**, 290–294 (2014).

[47]Z. Wang, Z. Dong, Y. Gu, Y.-H. Chang, L. Zhang, L.-J. Li, W. Zhao, G. Eda, W. Zhang, G. Grinblat, S. A. Maier, J. K. W. Yang, C.-W. Qiu, and A. T. S. Wee, "Giant photoluminescence enhancement in tungsten-diselenide-gold plasmonic hybrid structures", Nature Communications **7**, 11283 (2016).

[48]W. Gao, J. Shu, K. Reichel, D. V. Nickel, X. He, G. Shi, R. Vajtai, P. M. Ajayan, J. Kono, D. M. Mittleman, and Q. Xu, "High-contrast terahertz wave modulation by gated graphene enhanced by extraordinary transmission through ring apertures", Nano Letters **14**, 1242–1248 (2014).

[49]H.-T. Chen, W. J. Padilla, J. M. O. Zide, A. C. Gossard, A. J. Taylor, and R. D. Averitt, "Active terahertz metamaterial devices", Nature **444**, 597–600 (2006).

[50]W. Liu, Y. Shen, G. Xiao, X. She, J. Wang, and C. Jin, "Mechanically tunable sub-10nm metal gap by stretching PDMS substrate", Nanotechnology **28**, 075301 (2017).

[51]R. Xie, C. T. Bui, B. Varghese, Q. Zhang, C. H. Sow, B. Li, and J. T. L. Thong, "An electrically tuned solid-state thermal memory based on metal-insulator transition of single-crystalline VO2 nanobeams", Advanced Functional Materials **21**, 1602–1607 (2011).

[52]J. Zhu, K. Hippalgaonkar, S. Shen, K. Wang, Y. Abate, S. Lee, J. Wu, X. Yin, A. Majumdar, and X. Zhang, "Temperature-gated thermal rectifier for active heat flow control", Nano Letters **14**, 4867–4872 (2014).

[53]M. J. Martinez-Perez, A. Fornieri, and F. Giazotto, "Rectification of electronic heat current by a hybrid thermal diode", Nature Nanotechnology **10**, 303–307 (2015).

[54]P. BUFFAT and J. BOREL, "SIZE EFFECT ON MELTING TEMPERATURE OF GOLD PARTICLES", Physical Review A **13**, 2287–2298 (1976).

[55]G. Albrecht, S. Kaiser, H. Giessen, and M. Hentschel, "Refractory plasmonics without refractory materials", Nano Letters **17**, 6402–6408 (2017).

[56]M. Caldarola, P. Albella, E. Cortes, M. Rahmani, T. Roschuk, G. Grinblat, R. F. Oulton, A. V. Bragas, and S. A. Maier, "Non-plasmonic nanoantennas for surface enhanced spectroscopies with ultra-low heat conversion", Nature Communications **6**, 7915 (2015).

[57]"Engineeringtoolbox, linear thermal expansion coefficient, https://www.engineeringtoolbox.com/linear-expansion-coefficients-d_95.html (accessed: may 2018)",

[58]D. Aurbach, Y. Talyosef, B. Markovsky, E. Markevich, E. Zinigrad, L. Asraf, J. S. Gnanaraj, and H.-J. Kim, "Design of electrolyte solutions for li and li-ion batteries: a review", Electrochimica Acta **50**, 247–254 (2004).

[59]F. Cheng and J. Chen, "Metal–air batteries: from oxygen reduction electrochemistry to cathode catalysts", Chemical Society Reviews **41**, 2172 (2012).

[60]N. B. Aetukuri, B. D. McCloskey, J. M. García, L. E. Krupp, V. Viswanathan, and A. C. Luntz, "Solvating additives drive solution-mediated electrochemistry and enhance toroid growth in non-aqueous li–o2 batteries", Nature Chemistry **7**, 50–56 (2015).

[61]X. H. Liu and J. Y. Huang, "In situ TEM electrochemistry of anode materials in lithium ion batteries", Energy & Environmental Science **4**, 3844 (2011).

[62]Y.-X. Yin, S. Xin, Y.-G. Guo, and L.-J. Wan, "Lithium-sulfur batteries: electrochemistry, materials, and prospects", Angewandte Chemie International Edition **52**, 13186–13200 (2013).

[63]M. Huang, B. Xi, Z. Feng, F. Wu, D. Wei, J. Liu, J. Feng, Y. Qian, and S. Xiong, "New insights into the electrochemistry superiority of liquid na–k alloy in metal batteries", Small **15**, 1804916 (2019).

[64]E. D. Goluch, B. Wolfrum, P. S. Singh, M. A. G. Zevenbergen, and S. G. Lemay, "Redox cycling in nanofluidic channels using interdigitated electrodes", Analytical and Bioanalytical Chemistry **394**, 447–456 (2009).

[65]V. A. T. Dam, W. Olthuis, and A. van den Berg, "Redox cycling with facing interdigitated array electrodes as a method for selective detection of redox species", The Analyst **132**, 365 (2007).

[66]R. W. French, S. N. Gordeev, P. R. Raithby, and F. Marken, "Paired gold junction electrodes with submicrometer gap", Journal of Electroanalytical Chemistry **632**, 206–210 (2009).

[67]C. Ma, N. M. Contento, L. R. Gibson, and P. W. Bohn, "Redox cycling in nanoscale-recessed ring-disk electrode arrays for enhanced electrochemical sensitivity", ACS Nano **7**, 5483–5490 (2013).

[68]H. R. Zafarani, K. Mathwig, E. J. R. Sudhölter, and L. Rassaei, "Electrochemical amplification in side-by-side attoliter nanogap transducers", ACS Sensors **2**, 724–728 (2017).

[69]Y. Wang, J. G. Limon-Petersen, and R. G. Compton, "Measurement of the diffusion coefficients of [ru(NH3)6]3+ and [ru(NH3)6]2+ in aqueous solution using microelectrode double potential step chronoamperometry", Journal of Electroanalytical Chemistry **652**, 13–17 (2011).

[70]A. Walter, J. Wu, G.-U. Flechsig, D. A. Haake, and J. Wang, "Redox cycling amplified electrochemical detection of DNA hybridization: application to pathogen e. coli bacterial RNA", Analytica Chimica Acta **689**, 29–33 (2011).

[71]J. C. Byers, B. Paulose Nadappuram, D. Perry, K. McKelvey, A. W. Colburn, and P. R. Unwin, "Single molecule electrochemical detection in aqueous solutions and ionic liquids", Analytical Chemistry **87**, 10450–10456 (2015).

[72]S. Kang, A. F. Nieuwenhuis, K. Mathwig, D. Mampallil, Z. A. Kostiuchenko, and S. G. Lemay, "Single-molecule electrochemistry in nanochannels: probing the time of first passage", Faraday Discussions **193**, 41–50 (2016).

[73]Y. Wang, S. R. Narayanan, and W. Wu, "Field-assisted splitting of pure water based on deep-sub-debye-length nanogap electrochemical cells", ACS Nano **11**, 8421–8428 (2017).

[74]D. Han, L. P. Zaino, K. Fu, and P. W. Bohn, "Redox cycling in nanopore-conned recessed dual-ring electrode arrays", J. Phys. Chem. C **120**, 20634 (2016).

[75]C. Ma, N. M. Contento, and P. W. Bohn, "Redox cycling on recessed ring-disk nanoelectrode arrays in the absence of supporting electrolyte", J. Am. Chem. Soc. **136**, 7225 (2014).

[76]K. Fu, "Electrochemistry at single molecule occupancy in nanopore-confined recessed ring-disk electrode arrays", Faraday Discussions **193**, 51 (2016).

[77]M. A. G. Zevenbergen, B. L. Wolfrum, E. D. Goluch, P. S. Singh, and S. G. Lemay, "Fast electron-transfer kinetics probed in nanofluidic channels", Journal of the American Chemical Society **131**, 11471–11477 (2009).

[78]L. Rassaei, K. Mathwig, S. Kang, H. A. Heering, and S. G. Lemay, "Integrated biodetection in a nanouidic device", ACS Nano **8**, 8278 (2014).

[79]M. A. G. Zevenbergen, P. S. Singh, E. D. Goluch, B. L. Wolfrum, and S. G. Lemay, "Electrochemical correlation spectroscopy in nanouidic cavities", Analytical Chemistry **81**, 8203 (2009).

[80]B. Wolfrum, M. Zevenbergen, and S. Lemay, "Nanofluidic redox cycling amplification for the selective detection of catechol", Analytical Chemistry **80**, 972–977 (2008).

[81]K. Fu, D. Han, C. Ma, and P. W. Bohn, "Ion selective redox cycling in zero-dimensional nanopore electrode arrays at low ionic strength", Nanoscale **9**, 5164–5171 (2017).

[82]M. Huske, R. Stockmann, and B. Wolfrum, "Redox cycling in nanoporous electrochemical devices", Nanoscale **6**, 589 (2014).

[83]K. Williams, K. Gupta, and M. Wasilik, "Etch rates for micromachining processing-part II", Journal of Microelectromechanical Systems **12**, 761–778 (2003).

[84]N. Nioradze, R. Chen, J. Kim, M. Shen, P. Santhosh, and S. Amemiya, "Origins of nanoscale damage to glass-sealed platinum electrodes with submicrometer and nanometer size", Analytical Chemistry **85**, 6198–6202 (2013).

[85]H. R. Zafarani, K. Mathwig, E. J. Sudhölter, and L. Rassaei, “Electrochemical redox cycling in a new nanogap sensor: design and simulation”, Journal of Electroanalytical Chemistry **760**, 42–47 (2016).

[86]H. S. White and K. McKelvey, “Redox cycling in nanogap electrochemical cells”, Current Opinion in Electrochemistry **7**, 48–53 (2018).

국문초록

본 논문에서는 원자층 리소그래피 방식을 활용하여 내부가 빈 금속 나노갭을 제작하여 광학적 및 전기화학적으로 활용하는 방법에 대해서 탐구하였다. 먼저 나노갭 내부의 유전체 박막을 화학적으로 식각하고 에너지분산형 분광분석법 및 테라헤르츠파 분석을 통해 갭 내부가 완전히 비어 있음을 확인하였다. 다음으로 속이 빈 나노갭을 온도 변화에 따라 테라헤르츠파 투과특성 변화를 관측하여 능동적인 나노안테나로써 활용하였으며 그 원인이 온도 변화에 따른 금속의 열팽창으로 인한 것임을 확인하였다. 한편, 나노갭 내부의 유전체 박막을 식각하는 과정에서 물이 갭 내부에 채워질 수 있다는 사실을 발견하고 가장 폭이 작은 나노 전극으로 활용하여 산화환원반응의 증폭을 유도하였다. 본 연구에서 제시하는 나노갭 제작 방식을 통해 나노광학, 전기화학, 전기분광학 등 매우 다양한 분야에서 이러한 나노갭을 활용할 수 있는 가능성을 기대할 수 있다.

주요어: 나노갭, 열적 조작, 테라헤르츠파 변조, 산화환원반응, 패러데이 전류 증강

학번: 2014-21380